Quantitative estimation of effective viscosity in quantum turbulence

Vishwanath Shukla,[1,*] Pablo D. Mininni,[2,†] Giorgio Krstulovic,[3,‡] Patricio Clark di Leoni,[4,§] and Marc E. Brachet[5,‖]

[1]*Institut de Physique de Nice, Université de Côte d'Azur, CNRS, Nice, France*

[2]*Departamento de Física, Facultad de Ciencias Exactas y Naturales, Universidad de Buenos Aires and IFIBA, CONICET, Ciudad Universitaria, 1428 Buenos Aires, Argentina*

[3]*Université Côte d'Azur, Observatoire de la Côte d'Azur, CNRS, Laboratoire Lagrange, Bd de l'Observatoire, CS 34229, 06304 Nice cedex 4, France*

[4]*Department of Physics and INFN, University of Rome Tor Vergata, Via della Ricerca Scientifica 1, 00133 Rome, Italy*

[5]*Laboratoire de Physique Statistique de l'Ecole Normale Supérieure associé au CNRS et aux Universités Paris 6 et 7, 24 Rue Lhomond, 75237 Paris Cedex 05, France*

(Received 13 November 2018; published 4 April 2019)

We study freely decaying quantum turbulence by performing high-resolution numerical simulations of the Gross-Pitaevskii equation (GPE) in the Taylor-Green geometry. We use resolutions ranging from 1024^3 to 4096^3 grid points. The energy spectrum confirms the presence of both a Kolmogorov scaling range for scales larger than the intervortex scale ℓ, and a second inertial range for scales smaller than ℓ. Vortex line visualizations show the existence of substructures formed by a myriad of small-scale knotted vortices. Next, we study finite-temperature effects in decaying quantum turbulence by using the stochastic Ginzburg-Landau equation to generate thermal states, and then by evolving a combination of these thermal states with the Taylor-Green initial conditions under the GPE. We use finite-temperature GPE simulations to extract mean-free path by measuring the spectral broadening in the Bogoliubov dispersion relation that we obtain from the spatiotemporal spectra, and use it to quantify the effective viscosity as a function of the temperature. Finally, we perform low-Reynolds-number simulations of the Navier-Stokes equations, in order to compare the decay of high-temperature quantum flows with their classical counterparts, and to further calibrate the estimations of the effective viscosity (based on the mean-free-path computations).

DOI: 10.1103/PhysRevA.99.043605

I. INTRODUCTION

Turbulence in quantum fluids provides an exciting yet challenging scenario to explore multiscale and out-of-equilibrium dynamics. A turbulent state in superfluid ^{4}He was first envisioned by Feynman as a random interacting tangle of quantum vortex lines [1,2]. More recently, quantum turbulence has been realized and studied in experiments on a wide variety of superfluid systems [3], such as bosonic superfluid ^{4}He [4], its fermionic counterpart ^{3}He [5], and Bose-Einstein condensates (BECs) in traps [6]. It must be emphasized that the study of quantum turbulence in laboratory experiments is a challenging task, which requires measurements at very low temperatures and usually in small system sizes; therefore, any experimental progress relies heavily on technical advancements. This is where numerical and theoretical studies become important: first, by providing explanations for the experimental observations; and second, by probing regimes that are yet not directly accessible in current experimental setups. However, these approaches have limitations of their own.

Turbulent quantum fluids are known to display hydrodynamic behavior at the large scales, showcasing, for example, a Kolmogorov energy cascade [7,8]. At smaller scales, the dynamics is dominated instead by nonlinear interactions of Kelvin waves [9]. The crossover scale between these two regimes is determined by the mean intervortex length. Understanding how this picture is affected by finite-temperature effects is a subject of ongoing research. Currently, there is no single theory which covers all the systems and is capable of predicting the known dynamical effects across all the length scales and timescales. Therefore, much progress relies on phenomenological models, which at times are better suited for one type of problem than for others. There are three important classes of these phenomenological models: (i) the two-fluid models, (ii) the vortex filament model, and (iii) the Gross-Pitaevskii equation (GPE), also referred to as the nonlinear Schrödinger equation.

The phenomenological two-fluid model was proposed independently by Tisza and Landau to explain the superfluidity of ^{4}He below the lambda transition temperature. In this model, at subtransition temperatures ^{4}He is regarded as a physically inseparable mixture of the superfluid and normal fluid components. Many of the flow properties of superfluid helium at low velocities can be described within the framework of this model [10]. Among one of its great successes was the prediction of second sound in superfluid ^{4}He. However, it does not account for the presence

*research.vishwanath@gmail.com
†mininni@df.uba.ar
‡krstulovic@oca.eu
§patricio.clark@roma2.infn.it
‖brachet@physique.ens.fr

of quantum vortices, a very important feature of superfluid flows.

An extension of the two-fluid model is the Hall-Vinen-Bekharevich-Khalatnikov model [11,12]. This model incorporates the effect of interactions between the quantized vortices and the normal fluid by including a mutual friction term. In this model the distinction between individual vortices is ignored, and only length scales larger than the mean separation between quantum vortices are considered. Therefore, it is an effective, coarse-grained model, which provides a good description of superfluid turbulence at low Mach numbers. This model has been used to study large-scale flow properties and intermittency in direct numerical simulations (DNSs) of quantum turbulence [13–15] and in reduced dynamical systems based on shell models [16–19].

The vortex filament model [20] overcomes some of the limitations of the above two-fluid models by regarding the quantized vortices as filaments in three dimensions (3D), and evolving them under the Biot-Savart law plus a mutual friction term mimicking the coupling between the normal and superfluid components. However, vortex reconnection is taken care of on an *ad hoc* basis. This model is relevant in situations in which the core size is negligible in comparison to the characteristic length scales in the hydrodynamic description of the flow, e.g., the mean intervortex separation ℓ or the radius of curvature of the vortex filaments R; it has been used to study quantum turbulence at finite temperatures [21,22].

Finally, at zero or near-zero temperatures, for weakly interacting bosons the GPE provides a good hydrodynamical description of the superfluid flow; it naturally includes quantum vortices as exact solutions, which can reconnect without the need for any extra *ad hoc* assumptions [23]. The first 3D DNSs of decaying quantum turbulence, using the GPE as a model of a zero-temperature superfluid fluid, were performed some 20 years ago with linear resolutions up to $N = 512$ grid points in each spatial direction, in the geometry of the Taylor-Green (TG) vortex flow [7,24]. We recall that a freely decaying turbulence, starting with a suitable initial data, does not involve any external driving force. Moreover, forcing a superfluid by an external time-dependent field or by some stirrer typically excites a huge number of phonons, which may even overwhelm the vortex dynamics and the Kolmogorov turbulent regime. Therefore, it is natural to study a decaying superfluid turbulence starting from a suitable initial condition. Moreover, in the case of classical fluids, described by the Navier-Stokes equation, it is well known that when a Kolmogorov regime is present, the time evolution of the energy dissipation rises to a peak value, which is quite insensitive to the Reynolds number [25].

An important contribution of Refs. [7,24] was the introduction of a preparation method to generate initial data for the GPE that corresponds to the classical Taylor-Green initial data and generates vortex dynamics with minimal sound emission; also, for the diagnostics these studies proposed the decomposition of the total conserved energy into the incompressible kinetic energy and other energy components, each with their corresponding spectra. Physically, the main achievement of these works was to show that at the moment of maximum incompressible kinetic energy dissipation, the incompressible kinetic energy spectrum displays a power-law scaling which is compatible with Kolmogorov's $k^{-5/3}$ scaling. This scaling was later confirmed in both experimental [8] and numerical [26] studies. The GPE has also been used to study the small-scale Kelvin wave cascade [27,28], thereby, demonstrating that it is capable of capturing both the cascades.

More recently, high-resolution simulations resolving simultaneously the two inertial ranges (one for scales larger than the intervortex length and the other for smaller scales) were performed [29]. This study also showed that at large scales the GPE can reproduce the dual cascade of energy and helicity observed in classical turbulence [30].

However, a problem with the GPE framework is that finite-temperature effects are notoriously difficult to incorporate [31–33]. One minimalistic approach is to use the so-called classical field models [34], by spectrally truncating the GPE [35]. It is well known that the long time integration of the truncated system results in microcanonical equilibrium states and this approach captures the condensation transition [36]. This transition was later reproduced in Ref. [37] using a grand-canonical method, where it was shown to be a standard second-order λ transition. Moreover, dynamical counterflow effects on vortex motion, such as mutual friction and thermalization dynamics, were also shown to be correctly captured by this approach, and investigated in Refs. [37,38]. This scheme was also used to study the different regimes that appear during the relaxation dynamics of the turbulent two-dimensional (2D) GPE; here, the completely thermalized states exhibit Berezinskii-Kosterlitz-Thouless transition in the microcanonical ensemble framework [39,40]. This method was extended to compute the mutual friction coefficients in 2D [41].

Recently, this approach was used to study finite-temperature effects in helical quantum turbulence [42]. It was observed that close to the critical temperature, behavior of the truncated system is akin to a viscous classical flow; the incompressible kinetic energy decays exponentially in time. It was proposed that a quantitative estimation of the effective viscosity can be obtained by measuring the mean-free path of the thermal excitations directly on the spatiotemporal spectrum of the flow as a function of temperature; note that the spatiotemporal spectrum apparently also gives access to the spectrum of phonons in the system [27]. However, calculation of the spatiotemporal spectrum is computationally intensive; therefore, it is reasonable to perform it on a flow that maximizes the scale separation for given computational resources, for example, the TG vortex flow (because of its symmetries).

The purpose of this paper is thus twofold. First, we want to extend the zero-temperature ($T = 0$) TG vortex results at linear resolution $N = 512$, obtained 20 years ago, to the resolutions achievable with current computing resources. Second, we want to measure, at the highest possible spatial resolution, the spatiotemporal spectrum of the flow, in order to estimate the mean-free path and the associated effective viscosity.

The rest of the paper is organized as follows. In Sec. II we present the details of the GPE model and its numerical implementation. In particular, in Sec. II A we discuss the basic zero-temperature GPE theory and our diagnostics in terms of different energies and associated spectra. Section II B contains the details of our zero-temperature initial data preparation method. Our methods of incorporating finite-temperature

effects are reviewed in Sec. II C. We describe the numerical implementation of the problem in Sec. II D, and in Sec. II E we discuss the choice of units. Section III contains our results. First, in Sec. III A we present our results for zero-temperature GPE dynamics with linear spatial resolutions up to $N = 4096$. In Sec. III B we present the characterization of the finite-temperature GPE states, including the condensation transition. We give our results on the finite-temperature decaying GPE runs in Sec. III C. In Sec. III D we compute and discuss the truncated GPE spatiotemporal correlation and spectra. We evaluate the mean-free path in Sec. III E, and Sec. III F is devoted to the comparison of the finite-temperature freely decaying GPE runs with Navier-Stokes freely decaying runs. Finally, we present our conclusions in Sec. IV.

II. MODEL, INITIAL CONDITIONS, AND NUMERICAL METHODS

A. Gross-Pitaevskii theory

The GPE, a partial differential equation for a complex field ψ, describes the dynamics of a weakly interacting Bose gas at low temperatures. It reads as

$$i\hbar\frac{\partial\psi}{\partial t} = -\frac{\hbar^2}{2m}\nabla^2\psi + g|\psi|^2\psi, \tag{1}$$

where $|\psi|^2$ is the number of particles per unit volume, m is the mass of the bosons, $g = 4\pi\tilde{a}\hbar^2/m$, and $\tilde{a}$ is the s-wave scattering length. This equation conserves the total energy E, the total number of particles $\mathcal{N}_p$, and the momentum $\mathbf{P}$, defined in a volume V, respectively, as

$$E = \int_V d^3x\left(\frac{\hbar^2}{2m}|\nabla\psi|^2 + \frac{g}{2}|\psi|^4\right), \tag{2}$$

$$\mathcal{N}_p = \int_V |\psi|^2\, d^3x, \tag{3}$$

$$\mathbf{P} = \int_V \frac{i\hbar}{2}(\psi\nabla\overline{\psi} - \overline{\psi}\nabla\psi)\, d^3x, \tag{4}$$

where the overline denotes the complex conjugate.

Equation (1) can be mapped onto hydrodynamic equations of motion for a compressible irrotational fluid using the Madelung transformation given by

$$\psi(\mathbf{x},t) = \sqrt{\frac{\rho(\mathbf{x},t)}{m}}\exp\left[i\frac{m}{\hbar}\phi(\mathbf{x},t)\right], \tag{5}$$

where $\rho(\mathbf{x},t)$ is the fluid mass density and $\phi(\mathbf{x},t)$ is the velocity potential, which gives the fluid velocity $\mathbf{v} = \nabla\phi$. The Madelung transformation is singular on the zeros of ψ. As two conditions are required in the singular points (both real and imaginary parts of ψ must vanish), these singularities must take place on points in two dimensions (2D) and on curves in 3D. The Onsager-Feynman quantum of velocity circulation around the vortex lines ($\psi = 0$) is given by h/m.

An important property of quantum vortices is that the complex field ψ is regular at their positions. Their singularity is only present in the hydrodynamic variables and stems from the Madelung transformation (5). Indeed, when $\psi = 0$ the phase is not defined leading to the possibility of topological defects. The associated vorticity $\boldsymbol{\omega} = \nabla\times\mathbf{v}$ then reads as

$$\boldsymbol{\omega}(\mathbf{r}) = \frac{h}{m}\int ds\frac{d\mathbf{r}_0}{ds}\delta[\mathbf{r} - \mathbf{r}_0(s)], \tag{6}$$

where $\mathbf{r}_0(s)$ denotes the position of the vortex lines and s the arclength. The vorticity is thus a distribution concentrated on the quantum vortex lines and the velocity field $\mathbf{v}$ is ill behaved on these lines and has an incompressible (divergenceless) part that can be recovered from (6) by using a Biot-Savart integral.

When Eq. (1) is linearized around a constant state $\psi = A_0$, one obtains the Bogoliubov dispersion relation

$$\omega_B(k) = \sqrt{\frac{gk^2|A_0|^2}{m} + \frac{\hbar^2k^4}{4m^2}}. \tag{7}$$

The sound velocity is thus given by $c = \sqrt{g|A_0|^2/m}$, with dispersive effects taking place for length scales smaller than the coherence length defined by

$$\xi = \sqrt{\hbar^2/(2gm|A_0|^2)}; \tag{8}$$

ξ is also proportional to the radius of the vortex cores [7,24].

1. Energy decomposition and associated spectra

Following Refs. [7,24], we define the total energy per unit volume as $e_{\rm tot} = (E - \mu\mathcal{N}_p)/V - \mu^2/2g$, where μ is the chemical potential. We use the hydrodynamic fields to write $e_{\rm tot}$ as the sum of three components: the kinetic energy $e_{\rm kin}$, the internal energy $e_{\rm int}$, and the quantum energy $e_{\rm q}$ (all per unit volume), defined respectively as

$$e_{\rm kin} = \frac{1}{V}\int d^3x\frac{1}{2}(\sqrt{\rho}\mathbf{v})^2, \tag{9}$$

$$e_{\rm int} = \frac{1}{V}\int d^3x\frac{g}{2m^2}(\rho - \rho_0)^2, \tag{10}$$

$$e_{\rm q} = \frac{1}{V}\int d^3x\frac{\hbar^2}{2m^2}(\nabla\sqrt{\rho})^2, \tag{11}$$

where V is the volume of the system and $\rho_0 = m|A_0|^2$ is the mean mass density of the fluid. Furthermore, we decompose the kinetic energy into a compressible (irrotational) component $e^{\rm c}_{\rm kin}$ and an incompressible (rotational) component $e^{\rm i}_{\rm kin}$, by making use of the relation $\sqrt{\rho}\mathbf{v} = (\sqrt{\rho}\mathbf{v})^{\rm c} + (\sqrt{\rho}\mathbf{v})^{\rm i}$ with $\nabla\cdot(\sqrt{\rho}\mathbf{v})^{\rm i} = 0$ (see [7,24] for details).

We then use Parseval's theorem to construct corresponding energy spectra for each of these energies: e.g., the kinetic energy spectrum $e_{\rm kin}(k)$ is defined as

$$e_{\rm kin}(k) = \frac{1}{2}\int\left|\frac{1}{V}\int d^3r\, e^{i\mathbf{r}\cdot\mathbf{k}}\sqrt{\rho}\mathbf{v}\right|^2 k^2 d\Omega_k, \tag{12}$$

where $d\Omega_k$ is the solid angle element on the sphere in Fourier space.

This decomposition of the kinetic energy provides a practical way to separate in the spectrum, the incompressible contributions (produced by the quantum vortices) from the compressible ones (produced by the sound waves). Indeed, the 3D angle-averaged spectrum of a smooth isolated vortex line is known to be proportional to that of the 2D axisymmetric vortex, an exact solution of the GPE (1) given by $\psi^{\rm vort}(r) =$

$\sqrt{\rho(r)/m}\exp(\pm i\varphi)$ in polar coordinates (r,φ). The corresponding velocity field $v(r)=\frac{\hbar}{m}r^{-1}$ is azimuthal and the density profile, of characteristic spatial extent ξ, verifies $\sqrt{\rho(r)}\sim r$ as $r\to 0$ and $\sqrt{\rho(r)}=1+O(r^{-2})$ for $r\to\infty$. Thus, $\sqrt{\rho}v_j$ has a small r singular behavior of the type r^0 and behaves as r^{-1} at large r. In general, for a function scaling as $h(r)\sim r^s$ the (2D) Fourier transform is $\hat{h}(k)\sim k^{-s-2}$ and the associated spectrum scales as k^{-2s-3}. Thus, $E_{kin}(k)$ scales as k^{-3} for $k\gg k_\xi\sim\xi^{-1}$ and as k^{-1} for $k\ll k_\xi$. The k^{-1} behavior is characteristic of isolated vortices [7,24].

2. Vortex line length estimation

Working in a similar fashion as with the energy, we can define the incompressible momentum power spectrum

$$P^i(k)=\frac{1}{2}\int\left|\frac{1}{V}\int d^3r\, e^{i\mathbf{r}\cdot\mathbf{k}}(\rho\mathbf{v})^i\right|^2 k^2 d\Omega_k. \tag{13}$$

As was checked empirically in Refs. [7,24], the high-wave-number components of the incompressible part of this spectrum can be approximated, in two dimensions, as the sum of the momentum of all the vortices present in the flow counted individually. This fact provides an easy way to estimate the total line length of the vortices in a three-dimensional flow. One simply has to calculate the total incompressible momentum omitting the first wave numbers, and compare it to the momentum of a system where only one straight vortex line spanning the whole box length is present. As a result, the total vortex length L_V is

$$\frac{L_V}{2\pi}=\frac{\int_{k_{\min}}^{k_{\max}}P^i(k)dk}{\int_3^{k_{\max}}P^i_{\text{single}}(k)dk}, \tag{14}$$

where $k_{\max}$ is the maximum resolved wave number in the simulation, $k_{\min}$ is the lowest wave number not affected by the condensate (to be on the safe side it is usually taken to be equal to 3), $P^i_{\text{single}}(k)$ is the incompressible momentum power spectrum of a single vortex core (which can be calculated numerically by preparing the adequate initial conditions, or semianalytically by using an axisymmetric solution of the GPE, see [24]), and the factor 2π is the length of the computational domain. The average intervortex distance ℓ can finally be estimated from the total vortex length by looking at the vortex line density L_V/V in the following way:

$$\ell^{-2}=\frac{L_V}{V}. \tag{15}$$

B. Zero-temperature initial data preparation

The TG initial condition ψ_{TG} that will be used to study the free decay (no stirring force) of quantum turbulence in the GPE (1) is such that its nodal lines correspond to vortex lines of the so-called Taylor-Green flow. In dimensionless units, the TG velocity flow $\mathbf{u}_{\text{TG}}$ is defined as

$$\begin{aligned}u_x^{\text{TG}}(x,y,z)&=\sin(x)\cos(y)\cos(z),\\ u_y^{\text{TG}}(x,y,z)&=-\cos(x)\sin(y)\cos(z),\\ u_z^{\text{TG}}(x,y,z)&=0.\end{aligned} \tag{16}$$

1. Taylor-Green symmetries

The symmetries of the TG velocity field are rotational symmetries of angle π around the axes $x=z=\pi/2$, $y=z=\pi/2$, and $x=y=\pi/2$, and mirror symmetries with respect to the planes $x=0$ and π, $y=0$ and π, and $z=0$ and π. The TG velocity field is parallel to these planes, that form the sides of an *impermeable box* which confines the flow. It is demonstrated in Ref. [43] that when using $\mathbf{u}_{\text{TG}}$ as initial data for the Navier-Stokes equations, these symmetries are preserved by the dynamics, and that its solutions admit the following Fourier expansion:

$$\begin{aligned}u_x&=\sum_{m=0}^{\infty}\sum_{n=0}^{\infty}\sum_{p=0}^{\infty}\hat{u}_x(m,n,p)\sin mx\cos ny\cos pz,\\ u_y&=\sum_{m=0}^{\infty}\sum_{n=0}^{\infty}\sum_{p=0}^{\infty}\hat{u}_y(m,n,p)\cos mx\sin ny\cos pz,\\ u_z&=\sum_{m=0}^{\infty}\sum_{n=0}^{\infty}\sum_{p=0}^{\infty}\hat{u}_z(m,n,p)\cos mx\cos ny\sin pz,\end{aligned} \tag{17}$$

where $\hat{\mathbf{u}}(m,n,p)$ vanishes unless m,n,p are either all even or all odd integers. The expansion coefficients should also satisfy

$$\begin{aligned}\hat{u}_x(m,n,p)&=(-1)^{r+1}\hat{u}_y(n,m,p),\\ \hat{u}_z(m,n,p)&=(-1)^{r+1}\hat{u}_z(n,m,p),\end{aligned} \tag{18}$$

where $r=1$ when m,n,p are all even, and $r=2$ when m,n,p are all odd. These come from the fact that the TG flow has a rotational symmetry of angle of π around the axis $x=y=\pi/2$.

These symmetries can be extended to flows described by the GPE in Eq. (1). It is easy to show that the expressions in Eq. (17) applied to ρv_j, with $v_j=\partial_j\phi$ [see Eq. (5)], correspond to the following decomposition for the complex scalar $\psi(x,y,z,t)$ as a solution of the GPE:

$$\psi=\sum_{m=0}^{\infty}\sum_{n=0}^{\infty}\sum_{p=0}^{\infty}\hat{\psi}(m,n,p)\cos mx\cos ny\cos pz, \tag{19}$$

with $\hat{\psi}(m,n,p)=0$ unless m,n,p are either all even or all odd integers. The additional conditions then become

$$\hat{\psi}(m,n,p)=(-1)^{r+1}\hat{\psi}(n,m,p) \tag{20}$$

with the same convention as above. Implementing these relations in a numerical code yields savings of a factor 64 in computational time and memory size when compared to the general Fourier expansion.

2. Taylor-Green initial data

In order to create the initial condition ψ_{TG} with zeros along vortex lines of $\mathbf{u}_{\text{TG}}$, we make use of the Clebsch representation of the velocity field [7,24]. The Clebsch potentials

$$\begin{aligned}\lambda(x,y,z)&=\cos x\sqrt{2\,|\cos z|},\\ \mu(x,y,z)&=\cos y\sqrt{2\,|\cos z|}\,\operatorname{sgn}(\cos z)\end{aligned} \tag{21}$$

(where sgn is the sign function) generate the TG flow in Eq. (16), in the sense that $\nabla\times\mathbf{u}_{\text{TG}}=\nabla\lambda\times\nabla\mu$. Also, note

that a zero in the (λ, μ) plane corresponds to a vortex line of $\mathbf{u}_{\rm TG}$ (see [7,24] for details).

Defining the 2D complex field ψ_e with a simple zero at the origin of the (λ, μ) plane,

$$\psi_e(\lambda, \mu) = (\lambda + i\mu)\frac{\tanh(\sqrt{\lambda^2+\mu^2}/\sqrt{2}\xi)}{\sqrt{\lambda^2+\mu^2}}, \tag{22}$$

we obtain a three-dimensional field (as a function of x, y, and z) with one nodal line. We can further define

$$\psi_4(\lambda, \mu) = \psi_e\left(\lambda - \frac{1}{\sqrt{2}}, \mu\right)\psi_e\left(\lambda, \mu - \frac{1}{\sqrt{2}}\right), \times \psi_e\left(\lambda + \frac{1}{\sqrt{2}}, \mu\right)\psi_e\left(\lambda, \mu + \frac{1}{\sqrt{2}}\right), \tag{23}$$

which contains four nodal lines. In order to match the circulation of $\mathbf{u}_{\rm TG}$, we finally define a field which will be used below as initial condition for an equation for data preparation as

$$\psi_{\rm ARGLE}(x, y, z) = (\psi_4(\lambda(x, y, z), \mu(x, y, z)))^{[\gamma_d/4]}, \tag{24}$$

where the ratio of the total circulation to the elementary defect's circulation is $\gamma_d = (2/\pi)\hbar/(2m)$ with $\hbar/(2m) = c\xi/\sqrt{2}$ and the square brackets denote the integer part. Thus, initially each vortex line corresponds to a multiple zero line.

The final step in the initial data preparation method consists in running to convergence the advective real Ginzburg-Landau equation (ARGLE):

$$\frac{\partial\psi}{\partial t} = \frac{\hbar}{2m}\nabla^2\psi + \mu\psi - \frac{g}{\hbar}|\psi|^2\psi - i\mathbf{u}_{\rm TG}\cdot\boldsymbol{\nabla}\psi - \frac{|\mathbf{u}_{\rm TG}|^2}{2\hbar/m}\psi, \tag{25}$$

with the initial condition $\psi_{\rm ARGLE}$. The ARGLE evolution corresponds to the imaginary-time propagation of the GPE with a local Galilean transformation by the velocity field $\mathbf{u}_{\rm TG}$. Under ARGLE dynamics the multiple zero lines in $\psi_{\rm ARGLE}$ will spontaneously split into single zero lines, and the system will finally converge to initial conditions for the GPE, compatible with the TG flow, and with minimal sound emission. We denote the resulting converged state as $\psi_{\rm TG}$.

C. A finite-temperature model

One of the different possible ways to include finite-temperature effects on the condensate dynamics is by imposing an ultraviolet cutoff on the GPE. This amounts to performing a Galerkin truncation operation on the GPE in Fourier space with a projection operator $\mathcal{P}_{\rm G}$ defined as

$$\mathcal{P}_{\rm G}[\hat{\psi}(\mathbf{k})] = \Theta(k_{\rm max} - |\mathbf{k}|)\hat{\psi}(\mathbf{k}), \tag{26}$$

where $\hat{\psi}$ is the spatial Fourier transform of ψ, $k_{\rm max}$ is a suitably chosen ultraviolet cutoff (which, in practice, will be the same as the maximum resolved wave number in the simulations), and Θ is the Heaviside function. The resulting Galerkin truncated GPE (TGPE) is

$$i\hbar\frac{\partial\psi}{\partial t} = \mathcal{P}_{\rm G}\left[-\frac{\hbar^2}{2m}\nabla^2\psi + g\mathcal{P}_{\rm G}[|\psi|^2]\psi\right]. \tag{27}$$

The TGPE in Eq. (27) exactly conserves energy and mass; moreover, if we correctly dealias it by using the $\frac{2}{3}$ dealiasing rule [44], with $k_{\rm max} = \frac{2}{3}\times N/2$ (in dimensionless units), it also conserves momentum. We refer to Ref. [37] for an explicit demonstration of the latter. The Galerkin truncation operation also preserves the Hamiltonian structure with the truncated Hamiltonian of the system given by

$$H = \int d^3x\left[\frac{\hbar^2}{2m}|\boldsymbol{\nabla}\psi|^2 + \frac{g}{2}(\mathcal{P}_{\rm G}|\psi|^2)^2\right]. \tag{28}$$

The grand-canonical equilibrium states are given by the following stationary probability distribution:

$$\mathbb{P}_{\rm st}[\psi] = \frac{1}{\mathcal{Z}}e^{-\beta[H-\mu\mathcal{N}_p]}, \tag{29}$$

where $\mathcal{Z}$ is the grand partition function, $\beta = 1/(k_{\rm B}T)$ is the inverse temperature, and $k_{\rm B}$ is the Boltzmann constant. However, these states are difficult to compute as the Hamiltonians in Eqs. (2) or (28) are not quadratic, and the resulting statistical distribution is non-Gaussian. Nevertheless, it is possible to construct a stochastic process that converges to a stationary solution with equilibrium distribution given by Eq. (29). This process is defined by a Langevin equation consisting of a stochastic Ginzburg-Landau equation (SGLE) that explicitly reads as in physical space

$$\hbar\frac{\partial\psi}{\partial t} = \mathcal{P}_{\rm G}\left[\frac{\hbar^2}{2m}\nabla^2\psi + \mu\psi - g\mathcal{P}_{\rm G}[|\psi|^2]\psi\right] + \sqrt{\frac{2\hbar}{V\beta}}\mathcal{P}_{\rm G}[\zeta(\mathbf{x}, t)], \tag{30}$$

where the Gaussian white noise $\zeta(\mathbf{x}, t)$ obeys

$$\langle\zeta(\mathbf{x}, t)\overline{\zeta}(\mathbf{x}', t')\rangle = \delta(t - t')\delta(\mathbf{x} - \mathbf{x}'). \tag{31}$$

We refer to Ref. [37] for more details on the proof of the equivalence of this stationary probability distribution to the grand-canonical equilibrium state.

If one wants to control the number of particles $\mathcal{N}_p$ instead of the chemical potential μ, then one must supplement the SGLE with an *ad hoc* equation for the chemical potential

$$\frac{d\mu}{dt} = -\frac{\nu_N}{V}(\mathcal{N}_p - \mathcal{N}_p^*), \tag{32}$$

where $\mathcal{N}_p^*$ controls the mean number of particles and ν_N governs the rate at which SGLE equilibrates.

We will call the thermal states generated by the SGLE $\psi_{\rm th}$. These states can be used in the TGPE to compute their dynamical properties. Moreover, we can combine these thermal states with an initial condition for a large-scale flow to simulate quantum turbulence at finite temperature. For the TG flow, the combined initial state in this case reads as

$$\psi = \psi_{\rm TG}\times\psi_{\rm th}. \tag{33}$$

In this study, we perform several DNSs of the SGLE in Eq. (30) and of the TGPE in Eq. (27). For numerical purposes we rewrite the SGLE (omitting the Galerkin projector $\mathcal{P}_{\rm G}$) as

$$\frac{\partial\psi}{\partial t} = \alpha_0\nabla^2\psi + \Omega_0\psi - \beta_0|\psi|^2\psi + \sqrt{\frac{k_BT}{\alpha_0}}\zeta,$$

where α_0, Ω_0, and β_0 are parameters. We can express physically relevant quantities, such as the coherence length ξ and

the velocity of sound c, in terms of these new parameters. These are related by

$$\xi = \sqrt{\alpha_0/\Omega_0}, \qquad c = \sqrt{2\alpha_0\beta_0\rho_0}, \tag{34}$$

with $\rho_0 = \Omega_0/\beta_0$. In all the DNS runs presented below we set the density at $T = 0$ to $\rho_0 = 1$ (in dimensionless units as described below). In order to keep the value of intensive variables constant in the thermodynamic limit, at constant volume V and for $k_{\max} \to \infty$, the inverse temperature is expressed as $\beta = 1/(k_{\text{modes}}T)$, where $k_{\text{modes}} = V/\mathcal{N}_m$ with $\mathcal{N}_m$ the number of Fourier modes in the system. With these definitions, the temperature T has units of energy per volume, and $4\pi\alpha_0$ is the quantum of circulation.

D. Numerical implementation

The code TYGRS (TaYlor-GReen symmetric) is a pseudospectral code that enforces the symmetries of the TG vortex in 3D for the GPE, the Navier-Stokes equations, and the magnetohydrodynamic equations within periodic cubes of length 2π (in dimensionless units). As a result of the symmetries discussed in Sec. II B 1, the Fourier-transformed fields are nonzero only for wave vectors $(k_x, k_y, k_z) = (m, n, p)$ with jointly even or jointly odd components. Time integration of only these Fourier modes is performed using a fourth-order Runge-Kutta method with a fixed time step (see next subsection for details).

Pseudospectral codes are known to be optimal on periodic domains [44]. However, they require global spectral transforms, and thus are hard to implement in distributed memory environments, a crucial limitation until domain decomposition techniques (DDTs) arose [45,46] that allowed computation of serial fast Fourier transforms (FFTs) in different directions in space (local in memory) after performing transpositions. However, distributed parallelization using the message passing interface (MPI) in pseudospectral codes is limited in the number of processors that can be used, unless more transpositions are done per FFT (thus increasing communication time). To overcome this limitation, the hybrid (MPI-OPENMP) parallelization scheme that we have implemented in TYGRS builds upon a general purpose one-dimensional (slab-based) DDT that is effective for parallel scaling using MPI alone [47], extended with OPENMP to obtain (in practice) 2D DDT without the need of extra communication [48]. In this scheme, each MPI task creates multiple threads using OPENMP which operate over a fraction of the available data. This method has been extended in TYGRS to the sine (cosine) with even (odd) wave-number FFTs needed to implement the symmetries of TG flows, using loop-level OPENMP directives and multithreaded FFTs. The method was shown to scale with high parallel efficiency to over 100 000 CPU cores [48].

The runs were performed on the IDRIS BlueGene/P machine. At resolution $N = 4096$ we used 512 MPI processes, each process spawning 4 OPENMP threads, needing a total of 2048 CPU cores per simulation.

E. Units

In the following, all quantities are expressed in terms of a unit length L, a unit speed U, and a unit mass M. These are related to the simulation length L', the characteristic speed U', and the actual mass M' in the following way:

$$L = \frac{L'}{2\pi}, \tag{35}$$

$$U = \frac{U'}{2}, \tag{36}$$

$$M = \frac{M'}{(2\pi)^3}. \tag{37}$$

With these choices the simulation box is $2\pi L$ long (in each spatial direction), the speed of sound c is $2U$, and the mean density ρ_0 is equal to $1\,M/L^3$. The factors in Eqs. (35) to (37) result from the dimensionless scheme used in the simulations (done in a periodic box of dimensionless side 2π).

In this work we present simulations for $\xi k_{\max} = 1.5$, 2.5, and 4, a parameter that determines the healing length ξ. Therefore, in our simulation at the largest spatial resolution $N = 4096$ with $\xi k_{\max} = 2.5$, the healing length is $\xi \approx 0.0018L$. While the resolution in this simulation is state of the art, the scale separation is not sufficient to be able to compare with superfluid ^{4}He experiments, where the characteristic system size is $L' \approx 10^{-2}$ m, the speed of sound is $c' \approx 230$ m/s, the fluid density is ≈ 125 kg/m^3 (thus, $M' \approx 1.25 \times 10^{-4}$ kg), and the healing length is $\xi \approx 10^{-10}$ m $\approx 10^{-8}L'$ [3]. On the other hand, scale separation in BEC experiments of quantum turbulence, where $L' \approx 10^{-4}$ m, $c' \approx 2 \times 10^{-3}$ m/s, and $\xi \approx 5 \times 10^{-7}$ m $\approx 0.005L'$ [49,50], is within our reach.

The time step that we use in our simulations is prescribed by $dt = 1.6/N$ $[L/U]$, where N is the linear resolution. This allows us to conserve energy within a 2% error. We note that this error for a fourth-order Runge-Kutta method goes as the fourth power of dt; any attempt to improve accuracy by decreasing the time-step size increases the simulation cost, which goes as the inverse of dt. We also remind that the Galerkin truncated GPE and our spatial discretization scheme both conserve total energy and the numerical errors arise from the time discretization.

In this work, we express temperature in terms of the transition temperature T_λ, unless otherwise stated. Finally, we note that the intensity of nonlinear interactions is controlled by the inverse of $\xi k_{\max}$ [37]. Indeed, for $\xi k_{\max}$ very large, most of the excitations correspond to free particles.

For more details on the units in the DNSs of the GPE and SGLE, we refer to Refs. [24,37,38,42].

III. RESULTS

We start this section by discussing the temporal evolution of the TG flow at zero temperature based on state-of-the-art DNS at $N^3 = 4096^3$ and those at smaller number of collocation points. We then perform a series of temperature scans to study the decay of the TG initial conditions at finite temperatures. Finally, by computing the spatiotemporal spectra of these flows, we provide an estimation of the effective viscosity in flows evolved under the TGPE.

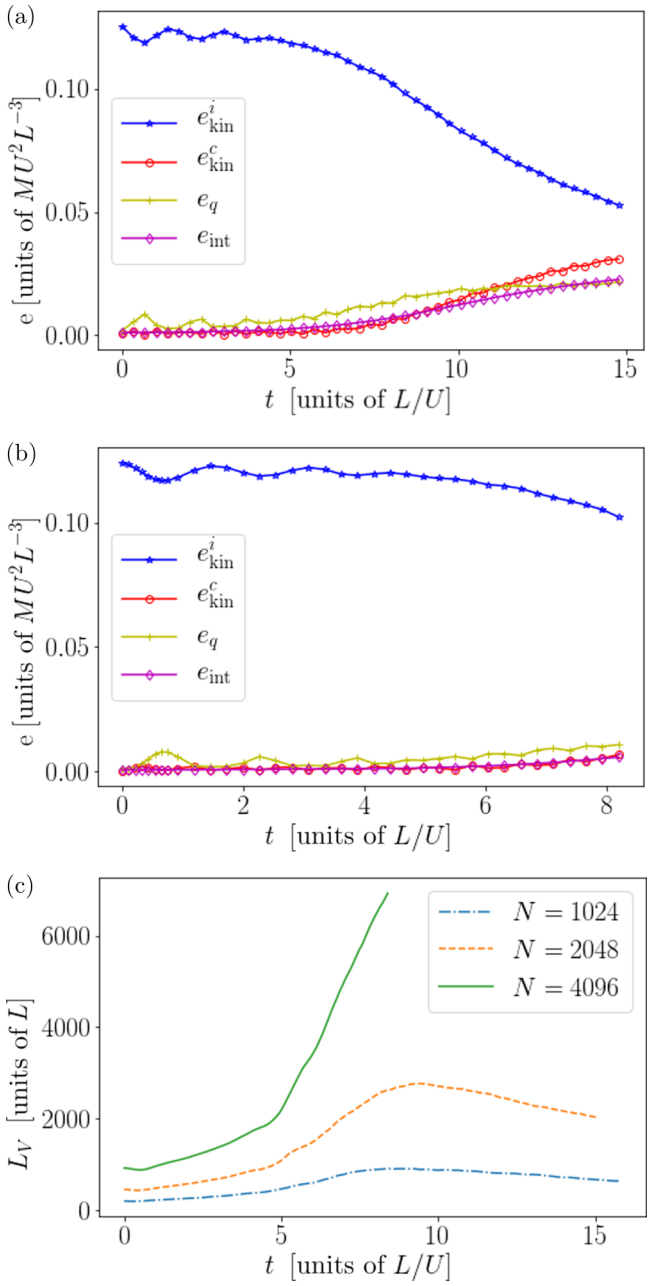

FIG. 1. Time evolution of the different energy components at zero temperature in (a) a 3D simulation with $N = 2048$ grid points in each spatial direction, and (b) with $N = 4096$ grid points in each direction. Both DNSs have $\xi k_{\rm max} = 2.5$. (c) Time evolution of the total vortex line length L_V in simulations at different spatial resolutions. The energy densities are given in units of MU^2L^{-3}, L_V is given in units of L, and t is in units of $[L/U]$.

A. High-resolution GPE runs at $T = 0$

We first prepare the TG initial data, following Eqs. (23)–(25), for $\xi k_{\rm max} = 2.5$ at linear spatial resolutions of $N = 1024$, 2048, and 4096. We then evolve this using the TGPE. In Figs. 1(a) and 1(b) we show the time evolution of the different energy (kinetic, quantum, and internal) components for the DNSs with $N = 2048$ and 4096 collocation points, respectively. In these simulations, the total energy was conserved within a 2% error. The incompressible kinetic energy per unit volume $e^i_{\rm kin}$ remains approximately constant until $t \approx 4\,L/U$, and afterward it starts decaying as the other energy components increase to keep the total energy fixed. This indicates a transfer of energy from $e^i_{\rm kin}$ to the other energy components as turbulence develops (most conspicuously at late times for the $N = 2048$ run, to the compressible component $e^c_{\rm kin}$). The vortex line length L_V, as defined in Eq. (14), is shown in Fig. 1(c) for all the three simulations. At around $t \approx 8\,L/U$, the simulations with $N = 1024$ and 2048 reach their maximum L_V, and thus the maximum of incompressible kinetic energy dissipation. The simulation with $N = 4096$ was stopped shortly before that point.

In Fig. 2(a) we show the incompressible kinetic energy spectra from the $N = 4096$ simulation at different times, while in Fig. 2(b) we present the same spectra at $t = 8\,L/U$ for the $N = 1024$, 2046, and 4096 simulations. Round markers indicate the mean intervortex wave number $k_\ell = 2\pi/\ell$, and the dashed lines indicate $k^{-5/3}$ power laws for a reference. On the one hand, at wave numbers smaller than k_ℓ, strong hydrodynamic turbulence is known to be the principal mechanism of energy transfer toward smaller scales. Therefore, a Kolmogorov-type spectrum is expected in this range of scales. On the other hand, at wave numbers larger than k_ℓ, energy is expected to be carried toward even smaller scales by the Kelvin wave cascade [9]. This cascade, predicted with weak-wave turbulence theory, also leads to a $k^{-5/3}$ scaling but with a different origin from the one of Kolmogorov. Note that the Kelvin wave cascade has been studied before using the GPE [51], and it has been observed in GPE turbulence using spatiotemporal analysis [27] and by direct measurement of vortex line excitations [28]. Also, it is known that the Kolmogorov and Kelvin wave cascades transfer the energy toward smaller scales at different rates. It is thus expected that energy should accumulate near the wave number k_ℓ, resulting in a bottleneck in the spectrum [52]. We indeed observe the emergence of a bottleneck in the vicinity of this wave number although not as pronounced as the thermalization scaling $\sim k^2$. This difference might be due to the fact that the present simulations correspond to freely decaying turbulence rather than one in a steady state with an external forcing. The existence of two simultaneous inertial ranges separated by a bottleneck was also observed before in high-resolution simulations using different initial conditions [29], but was not visible in the $N = 512$ DNS of a TG flow in [24] possibly because of a limited spatial resolution in that study. To further illustrate these ranges and the scale separation involved, in Figs. 2(c) and 2(d) we show the incompressible kinetic energy spectra compensated by Kolmogorov scaling $\sim k^{-5/3}$.

Visualizations of the vortex lines in the $N = 4096$ run close to the time of maximum energy dissipation are shown in Fig. 3. The intricate vortex line tangle in the entire computational domain (for the TG *impermeable box*) is shown first. The large-scale flow shows inhomogeneous regions with high density of vortices and quiet regions with low density. Details into the central regions with high density of vortices (and large shear) are also shown. It should be noted that the tangle of vortices results from many reconnections taking place after $t \approx 4\,L/U$. Comparing these $N = 4096$ results with those obtained 20 years ago at resolution $N = 512$ and presented in

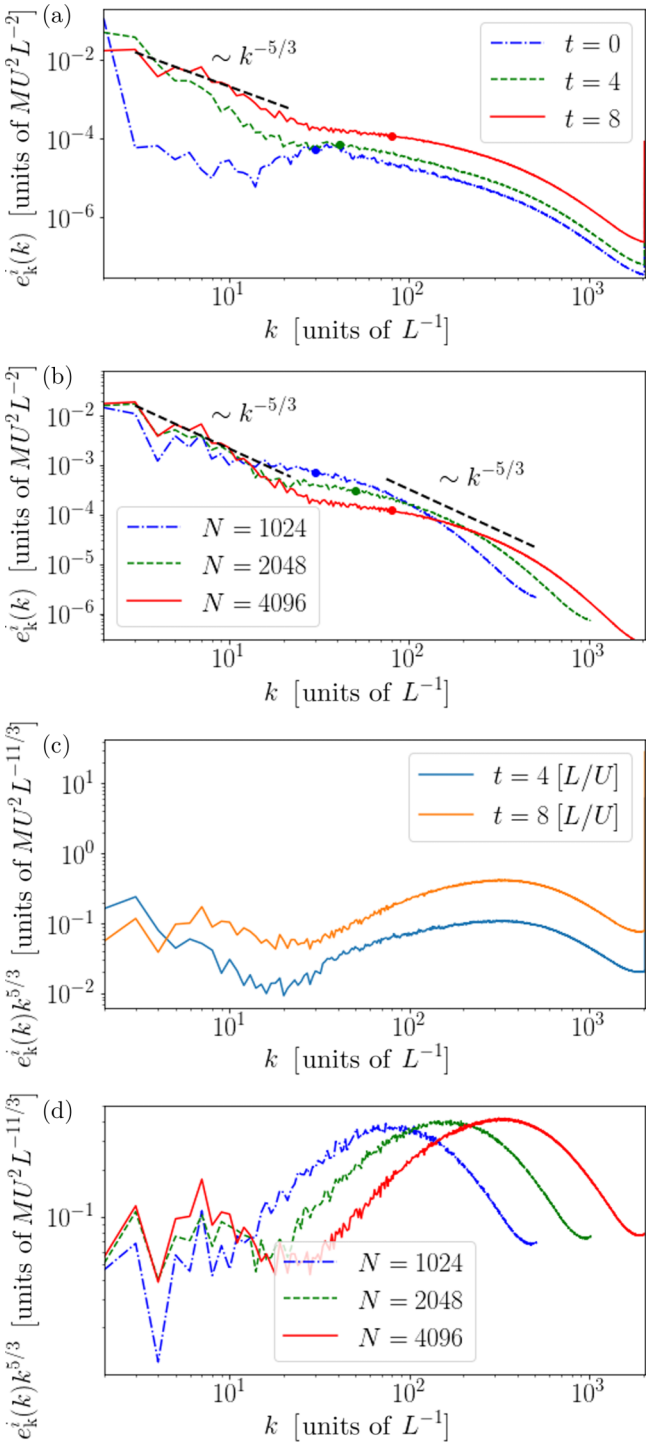

FIG. 2. (a) Incompressible kinetic energy spectra $e^i_{\rm kin}(k)$ at zero temperature, at different times for the $N = 4096$ simulation. (b) Spectra at $t = 8$ for three DNSs at different spatial resolution. In both panels, the circular marks indicate the mean intervortex wave number at the corresponding time, or for the corresponding spatial resolution. Power laws $\sim k^{-5/3}$ are shown as a reference, for scales larger and smaller than the intervortex scale. Note the emergence of a second inertial range, after a bottleneck, for scales smaller than the intervortex scale. (c), (d) Show the spectra from (a) and (b), but compensated by Kolmogorov scaling. The energy spectra are given in units of MU^2L^{-2}, the compensated spectra are in units of $MU^2L^{-11/3}$, and k is in units of L^{-1}.

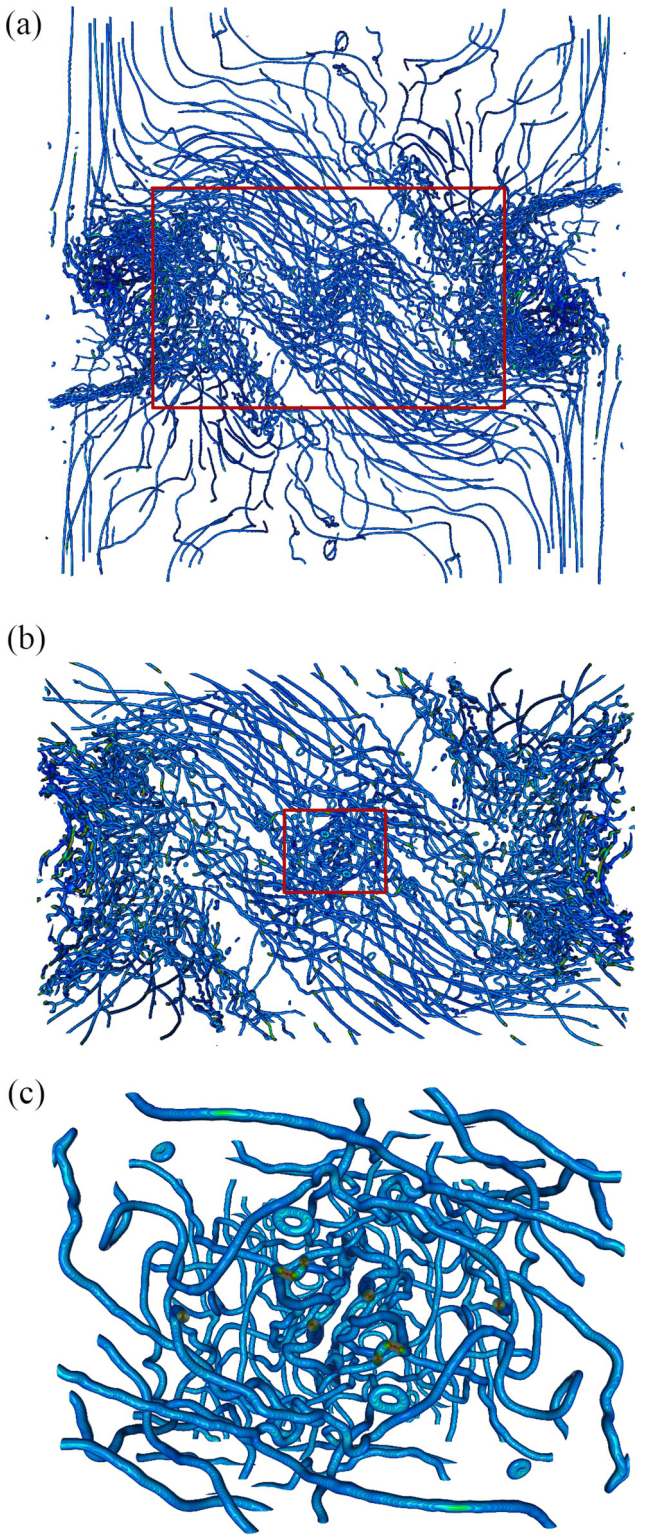

FIG. 3. Three-dimensional renderings of vortex lines at the onset of the decay in the 4096^4 GPE run. (a) The full impermeable box. The (red) box indicates the region shown in (b), which shows a zoom into a region of the domain with large shear of the vortex lines. Again, the (red) box in this panel indicates the region zoomed into in (c). Note in the latter panel the tangle of vortices, the many links between vortices, and the helical deformations of individual vortices along the vortex line. Visualizations were prepared using the software VAPOR [53].

TABLE I. Transition energy $e_\lambda = E_\lambda/V$, and temperature T_λ in the phase transition, for sets of runs at different spatial linear resolution N, and with different values of $\xi k_{\max}$. Values of the energies and temperatures are in units of MU^2L^{-3}.

	Resolution		
$\xi k_{\max}$	$N = 128$	$N = 256$	$N = 512$
1.5		$e_\lambda = 4.17$ $T_\lambda = 3.25$	
2.5	$e_\lambda = 10.64$ $T_\lambda = 9.5$	$e_\lambda = 10.13$ $T_\lambda = 9.25$	$e_\lambda = 9.12$ $T_\lambda = 8.75$
4		$e_\lambda = 24.12$ $T_\lambda = 23.5$	

Fig. 18 of Ref. [24], we can note the presence of substructures made by a myriad of small-scale and knotted and linked vortices that were not apparent at the lower resolution.

B. SGLE temperature scans

We now compute the thermal states, in order to determine the condensation transition temperature T_λ for our system with symmetries. To do so, we perform a series of SGLE temperature scans for various values of the linear resolution N and $\xi k_{\max}$ (see Table I). Each row of the table displays the transition energy and temperature that we obtain for a fixed N and $\xi k_{\max}$ by performing 12 to 24 simulations by varying the temperature. Boxes without data correspond to cases that we have not explored.

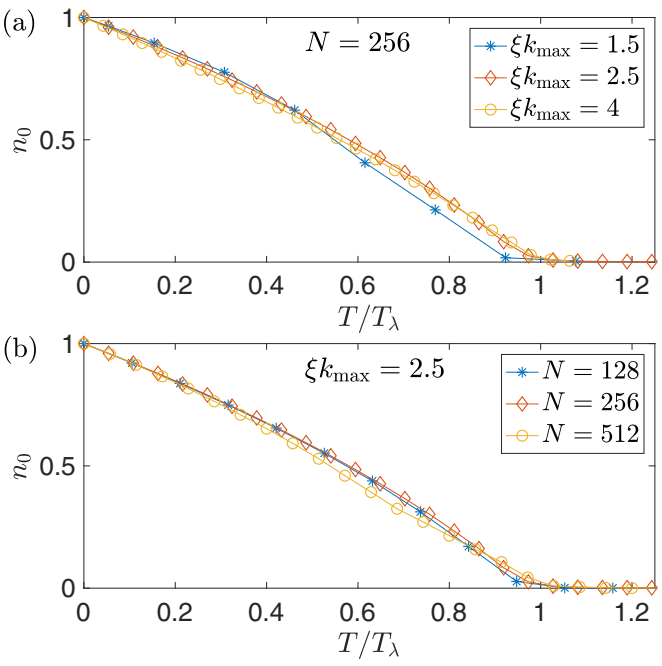

FIG. 4. (a) Condensate fraction as a function of T/T_λ at linear resolution $N = 256$ and for different values of $\xi k_{\max}$. (b) Condensate fraction as a function of T/T_λ at $\xi k_{\max} = 2.5$ and for different linear resolutions N. The condensate fraction is computed using Eq. (38) with $k_c = 2$ for simulations with $N = 128$, and with $k_c = 4$ for all the other numerical simulations.

It is well known that the TGPE can capture the condensation transition [34,36,37]. The order parameter of this phase transition is the condensate fraction, which is usually defined as the fraction of atoms that are in the ground state. In terms of Fourier modes, it is given by $|\hat{\psi}(\mathbf{k} = 0)|^2/\mathcal{N}_p$. However, for the TG flow the symmetries cancel exactly the energy (and mass density) of some Fourier modes, decreasing the availability of Fourier modes at low wave numbers, and thus affect the dynamics of the condensate fraction. To take this into account, we define the condensate fraction as

$$n_0 = \frac{1}{\mathcal{N}_p} \int_{k=0}^{k_c} |\widehat{\psi}_{\mathbf{k}}|^2 k^2 d\Omega_k, \tag{38}$$

where k_c is a small wave number (either 2 or 4, in dimensionless units, depending on the spatial resolution N).

In Figs. 4(a) and 4(b) we show the condensate fraction as a function of temperature for three different values of $\xi k_{\max}$ (1.5, 2.5, and 4 at $N = 256$) and N (128, 256, and 512 for $\xi k_{\max} = 2.5$), respectively. In each of these cases we identify the transition temperature by $T/T_\lambda = 1$.

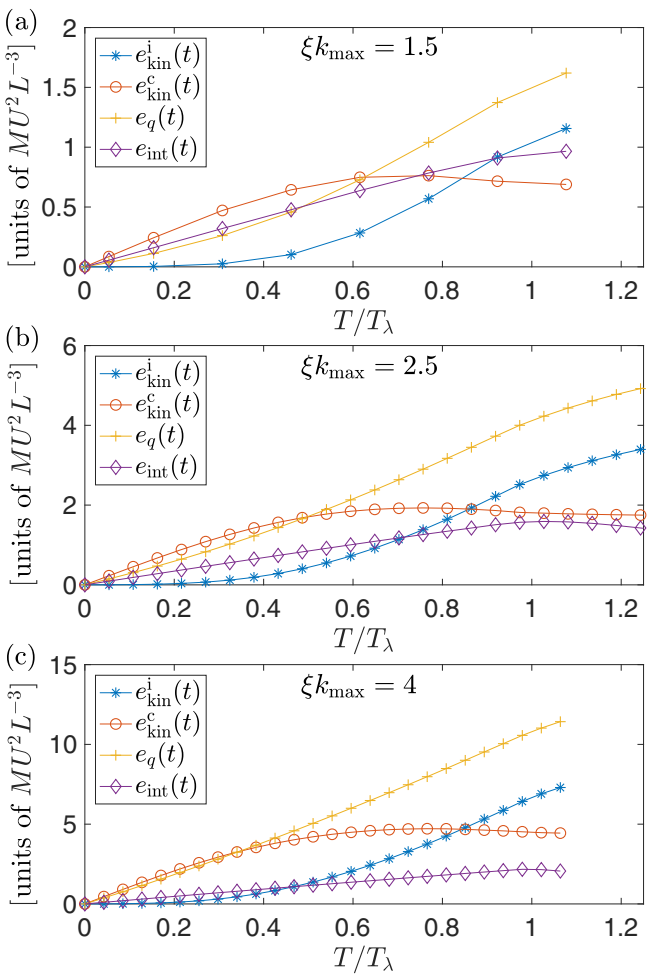

FIG. 5. Energy components as a function of the temperature, for different values of $\xi k_{\max}$, and for fixed linear spatial resolution ($N = 256$). (a) Temperature scan with $\xi k_{\max} = 1.5$, (b) same with $\xi k_{\max} = 2.5$, and (c) same with $\xi k_{\max} = 4$. The energy densities are given in units of MU^2L^{-3}, and the time is in units of L/U.

TABLE II. Variation of the total energy $e_{\rm tot}$ and of the condensate fraction n_0 in the thermal runs with $N = 1024$ and $\xi k_{\rm max} = 2.5$ (for these parameters $T_\lambda = 8.58$, in units of MU^2/L^3).

T/T_λ	$e_{\rm tot}$ (units of MU^2/L^3)	n_0
0	0.129	1
0.11	0.95	0.92
0.22	1.94	0.86
0.33	2.96	0.75
0.44	4.02	0.65
0.55	5.14	0.55

Moreover, in Figs. 5(a)–5(c) we show the behavior of the energy components as a function of temperature for $\xi k_{\rm max} = 1.5$, 2.5, and 4, respectively, at a fixed linear spatial resolution $N = 256$. We find that for a fixed $\xi k_{\rm max}$, the energy components $e_{\rm q}$, $e_{\rm int}$, and $e^i_{\rm kin}$ increases with T up to T_λ, whereas $e^c_{\rm kin}$ displays a maximum at intermediate temperatures. Also, as expected, increasing the value of $\xi k_{\rm max}$ decreases the nonlinear interaction strength, which can be quantified by the relative value of $e_{\rm int}(t)$.

A comparison of these results (simulations with TG symmetric flow) with those obtained for a general periodic geometry (see Fig. 2 of Ref. [37]) suggests that the overall properties of the condensation transition are not significantly affected by the nature of the geometry imposed by the symmetries at the largest scale. This motivates us to further investigate the turbulent dynamics at finite temperatures produced by combining the thermal states with the TG flow.

C. Thermal equilibria combined with the TG flow

To study finite-temperature effects, we first prepare a thermal state and then combine it with the zero-temperature TG (Taylor-Green) flow to finally generate a finite-temperature initial data for the TGPE evolution. In this section we present our results from the simulations with $N = 1024$ and $\xi k_{\rm max} = 2.5$ (see Table II for more details).

We begin with the discussion of how finite-temperature effects influence the temporal evolution of the energy components $e^i_{\rm kin}$, $e^c_{\rm kin}$, $e_{\rm q}$, and $e_{\rm int}$. For a comparative study, we show the time evolution of these energy components in Figs. 6(a)–6(d) for four different values of temperature $T = 0$, $0.11\,T_\lambda$, $0.33\,T_\lambda$, and $0.55\,T_\lambda$, respectively. We find that at $T = 0$ [Fig. 6(a)] the incompressible kinetic energy stays roughly constant until $t \approx 5\,L/U$, followed by a strong decay, which is almost 30% of its initial value, in an equal interval of time (up to $t \approx 10\,L/U$); thereafter, its decay slows down. This behavior is consistent with the $T = 0$ simulations at $N = 2048$ and 4096. The decrease in $e^i_{\rm kin}$ during the initial phase of the dynamical evolution is accompanied by an increase in the other components of energy, with $e_{\rm int}$ gaining the maximum share until $t \approx 10\,L/U$, after which it saturates. At later stages, the compressible kinetic energy is the most dominant component.

The plots of the energy components $e^c_{\rm kin}$, $e_{\rm q}$, and $e_{\rm int}$ in Figs. 6(c) and 6(d) show that at finite temperatures these start at higher values than their $T = 0$ counterparts; this is in agreement with our discussion in Sec. III B (see Fig. 5). We also observe that for the simulations at $T = 0.33T_\lambda$ and $0.55T_\lambda$, $e^i_{\rm kin}$ has the lowest share of the total energy, while

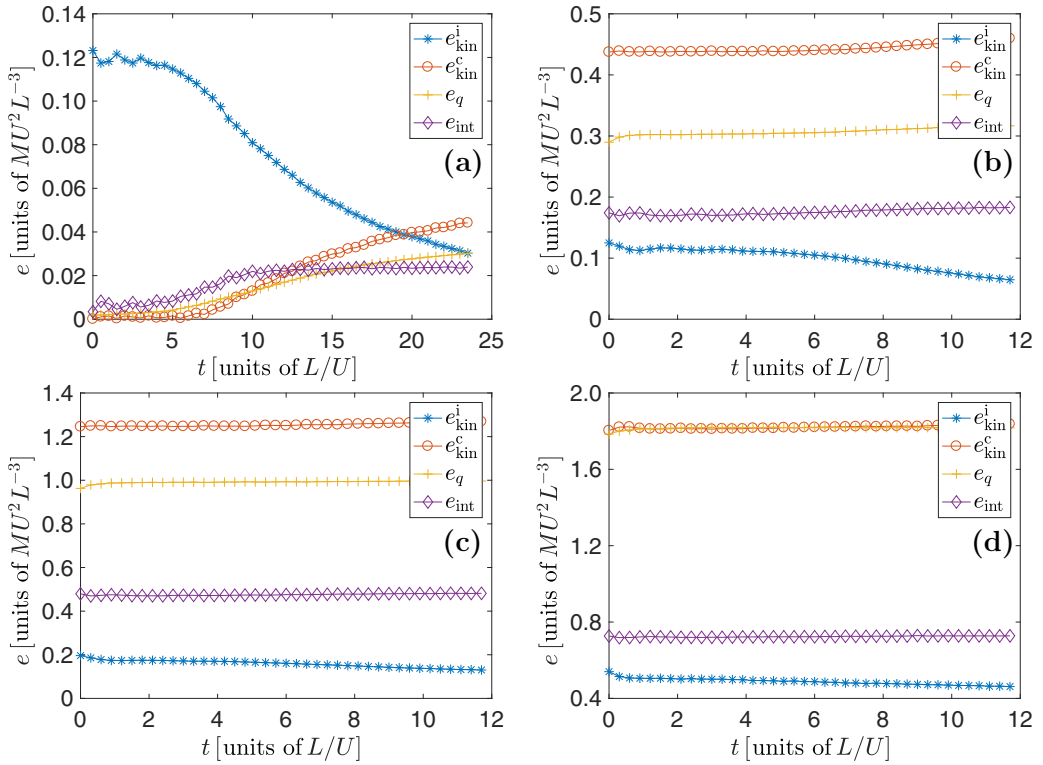

FIG. 6. Time evolution of the energy components in the TGPE runs with linear spatial resolution $N = 1024$ and $\xi k_{\rm max} = 2.5$ at four different temperatures: (a) $T = 0\,T_\lambda$, (b) $0.11\,T_\lambda$, (c) $0.33\,T_\lambda$, and (d) $0.55\,T_\lambda$.

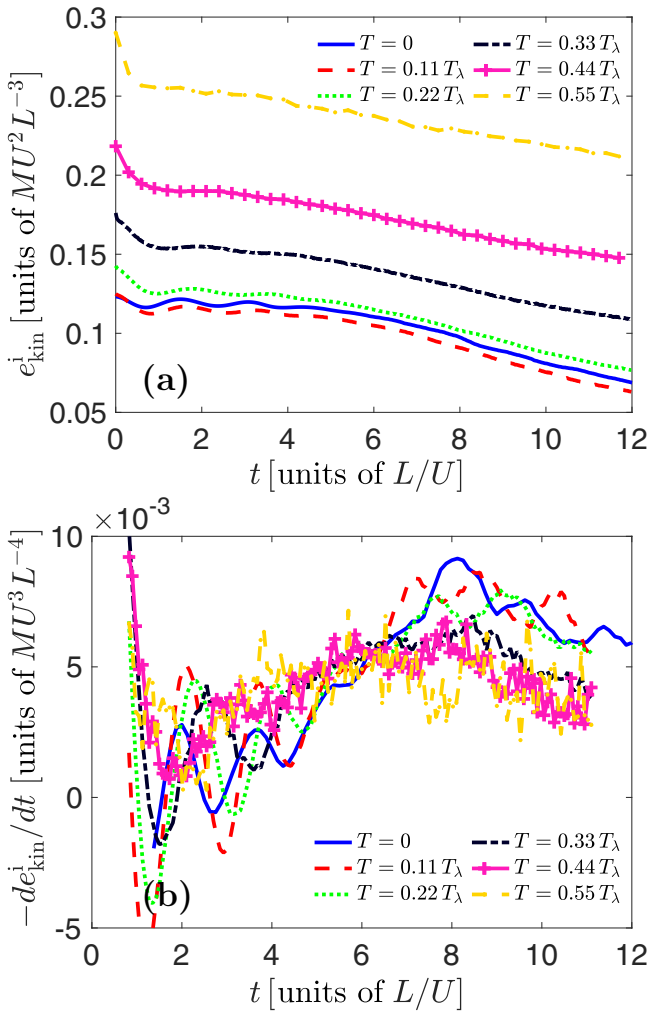

FIG. 7. Time evolution of (a) the incompressible kinetic energy $e^i_{\rm kin}$, and of (b) the incompressible kinetic energy dissipation rate $-de^i_{\rm kin}/dt$, at six different temperatures in TGPE runs with linear spatial resolution $N = 1024$ and $\xi k_{\rm max} = 2.5$. The incompressible kinetic energy is given in units of MU^2L^{-3}, its time derivative in units of MU^3L^{-4}, and the time is in units of L/U.

$e^c_{\rm kin}$ is generally the dominant component; however, at $T = 0.55\,T_\lambda$, $e_{\rm q}$ is comparable to the latter.

Irrespective of these differences during the initial stages, we find that the temporal evolution of $e^i_{\rm kin}$ is qualitatively similar for all the cases presented in Fig. 6. For a better comparison, we show in Fig. 7(a) the time evolution of $e^i_{\rm kin}$ at five different temperatures; these plots suggest that except for the initial adaptation period that lasts up to $t \approx 1\,L/U$, the incompressible kinetic energy decreases very slowly during the time interval $t \approx 2\,L/U$ to $4\,L/U$, in which it is roughly constant for the $T = 0$ case, followed by a fast decay of $e^i_{\rm kin}$.

We quantify this behavior by computing the decay rate $-de^i_{\rm kin}/dt$, a quantity that is frequently studied in freely decaying classical fluid turbulence. In Fig. 7(b) we show the temporal evolution of $-de^i_{\rm kin}/dt$ for different temperatures. If we discard the initial adaptation period, then we observe that the low temperature (up to $T = 0.44\,T_\lambda$) curves exhibit a peak at $t \approx 8\,L/U$; the peak value decreases as we increase the temperature and locally the curves become flat. At higher temperatures, $-de^i_{\rm kin}/dt$ exhibits strong fluctuations, e.g., for $T = 0.55\,T_\lambda$ it fluctuates about $5 \times 10^{-3} MU^3L^{-4}$ and we are unable to make more precise estimates. Note that given these fluctuations, we first perform a filtering operation to smooth out the curves, before computing the quantity of interest. It is also interesting to note that at about $t \approx 8\,L/U$ the vortex line length L_V is maximum for the $T = 0$ runs [see Sec. III A and Fig. 1(c)].

To understand how thermal fluctuations affect the dynamics across the length scales during the evolution of the TG flow toward a turbulent state, in Figs. 8(a)–8(d) we show the incompressible and compressible kinetic energy spectra for four different values of temperature $T = 0$, $T = 0.11\,T_\lambda$, $0.33\,T_\lambda$, and $0.55\,T_\lambda$, respectively; we show these for the instant of time at which observe a self-similar scaling range on the incompressible kinetic energy spectra. We observe that for the $T = 0$ case [Fig. 8(a)], $e^i_{\rm kin}(k) \sim k^{-5/3}$ scaling at small wave numbers (roughly over a decade) is followed by a bottleneck at about $k \approx 20\,L^{-1}$ and an exponential decay at high wave numbers. $e^c_{\rm kin}(k)$ is almost negligible compared to $e^i_{\rm kin}(k)$ at this instant of time. We find $e^i_{\rm kin}(k) \sim k^{-5/3}$ scaling region at finite temperatures as well, but now at high wave numbers we also see an accumulation of energy and the development of a thermalized region; this indicates that the small-scale fluctuations become more energetic as we increase the temperature. Simultaneously, the amplitude of $e^c_{\rm kin}(k)$ increases with increasing T and we observe the expected $e^c_{\rm kin}(k) \sim k^2$ scaling at high wave numbers. We also find that at $T = 0.55\,T_\lambda$ [see Fig. 8(d)], $e^i_{\rm kin}(k)$ no longer exhibits a Kolmogorov scaling over a significant range. The crossover wave number $k \approx 20L^{-1}$ in the $T = 0$ case, where the inertial range ends, is strongly modified in this run by the thermal bath at high wave numbers that now extends to smaller wave numbers, thereby reducing the inertial range.

Finally, to illustrate the time evolution of the spectra, we show in Fig. 9 the incompressible and compressible kinetic energy spectra for the temperatures $T = 0$ and $0.33\,T_\lambda$ at different instants of time. We observe a development of the the Kolmogorov scaling region at small wave numbers on the incompressible kinetic energy spectra, whereas the compressible component exhibits $e^c_{\rm kin} \sim k^2$ scaling at all times. We refer to videos M1 ($T = 0$) and M2 ($T > 0$) in the Supplemental Material [54] for the complete time evolution of these spectra.

D. TGPE spatiotemporal spectra in thermal equilibrium

To complete the quantification of thermal effects, in this section we compute and describe the spatiotemporal spectra (STS) of ψ for some of our SGLE equilibrium runs listed in Table I. We need these to estimate the mean-free path and effective viscosity.

STS provides the power spectrum of a given quantity as a function of wave number and frequency [27,55,56]. To compute this spectrum, we must store the quantity of interest very frequently, i.e., at very small intervals of time, if we want the Fourier transform in time to resolve the relevant high frequencies involved in the problem. This is computationally very challenging, if the linear resolution N is large. The resulting spectrum describes the amplitude of excitations as

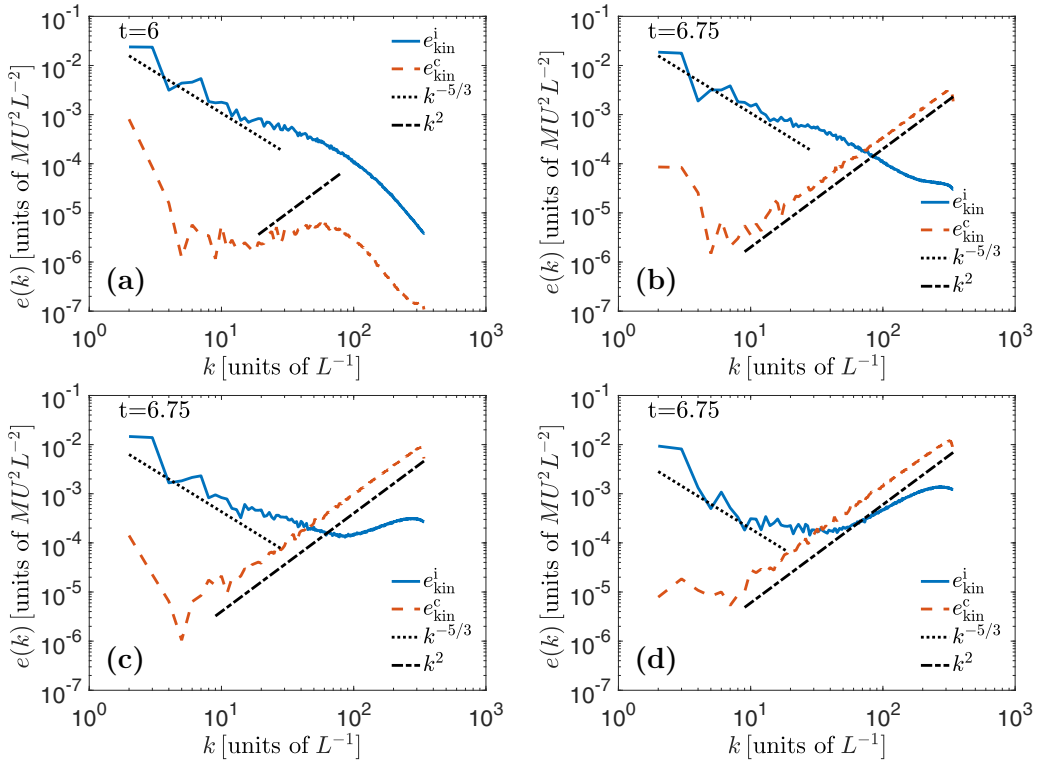

FIG. 8. Kinetic energy spectra $e^i_{\rm kin}(k)$ and $e^c_{\rm kin}(k)$ for four different temperatures: (a) $T = 0\,T_\lambda$, (b) $0.11\,T_\lambda$, (c) $0.33\,T_\lambda$, and (d) $0.55\,T_\lambda$, from TGPE runs with linear spatial resolution $N = 1024$ and $\xi k_{\rm max} = 2.5$. Videos M1 ($T = 0$) and M2 ($T > 0$) (see Supplemental Material [54]) show the time evolution of the compensated incompressible kinetic energy spectra at different temperatures. The energy spectra are in units of MU^2L^{-2} and k in units of L^{-1}.

a function of k and ω; this then can be used to extract information about the waves in a disordered state. For example, the STS of ψ gives information about the mass fluctuations.

In Fig. 10 we show the STS at different values of temperature both below and above T_λ from our simulations with $N^3 = 256^3$ and $\xi k_{\rm max} = 1.5$. At very low temperatures, e.g., $T = 0.05T_\lambda$ (see Fig 10), nonlinear interaction is very weak and leads to exact resonances in the periodic domain and only those modes are excited that satisfy the Bogoliubov dispersion relation given by Eq. (7); we show the latter by green dashed lines on the plots. We remark that the modes with $\omega = 0$ correspond to the condensate. A comparative study of different plots in Fig. 10 shows that as we increase the temperature, the nonlinear interactions become important and the dispersion curve broadens, e.g., at $T = 0.31T_\lambda$. We also note that at higher temperatures the condensate, which appears as horizontal straight line, shifts to higher frequencies, as it now satisfies $\hbar\omega = \mu$. The excitation of sound waves and the associated broadening about the Bogoliubov dispersion curve keeps increasing as we increase the temperature toward T_λ; this is expected as the broadening should be strongest close to the transition. For temperatures larger than T_λ, the dispersion relation switches to that of free particles and we expect to recover the standard four-wave interaction. Moreover, at $T = 1.08T_\lambda$ the horizontal straight line corresponding to the condensate completely disappears.

In Fig. 11 we show the STS at different temperatures from simulations with $\xi k_{\rm max} = 2.5$. As expected, the qualitative behavior is similar to the case of $\xi k_{\rm max} = 1.5$. However, at a fixed temperature now the spectral broadening is smaller; this is consistent with the fact that at large $\xi k_{\rm max}$ the nonlinear interaction is expected to be weaker.

We define spectral broadening $\Delta\omega(k)$ at each k as the width over which the power (about the dispersion curve) drops to half of its maximum amplitude. We recall that the inverse of $\Delta\omega(k)$ provides us with a measure of the nonlinear interaction time. In Fig. 12 we show the plots of $\Delta\omega(k)$ vs k at different temperatures for three values of $\xi k_{\rm max}$. A summary of important features that we observe from these plots is as follows: (1) at fixed temperature $\Delta\omega(k)$ increases with k and reaches its maximum value at $k \sim 1/\xi$, beyond which it either grows slowly or remains approximately constant; (2) at fixed k, $\Delta\omega(k)$ increases with temperatures and attains its maximum value close to T_λ; (3) the magnitude of $\Delta\omega(k)$ significantly decreases with increase in $\xi k_{\rm max}$, thereby confirming that the latter controls the strength of nonlinear interactions.

E. Mean-free path and effective viscosity

In this section we provide our estimates of the mean-free path and effective viscosity for the TGPE flow at finite temperatures. As mentioned above, the inverse of $\Delta\omega$ is associated with the nonlinear interaction time, during which the waves present in the system propagate without being scattered by other waves [57]. Therefore, we compute the mean-free path as follows:

$$\lambda(k, T) \sim \frac{1}{\Delta\omega(k, T)} \frac{d\omega_B}{dk}. \tag{39}$$

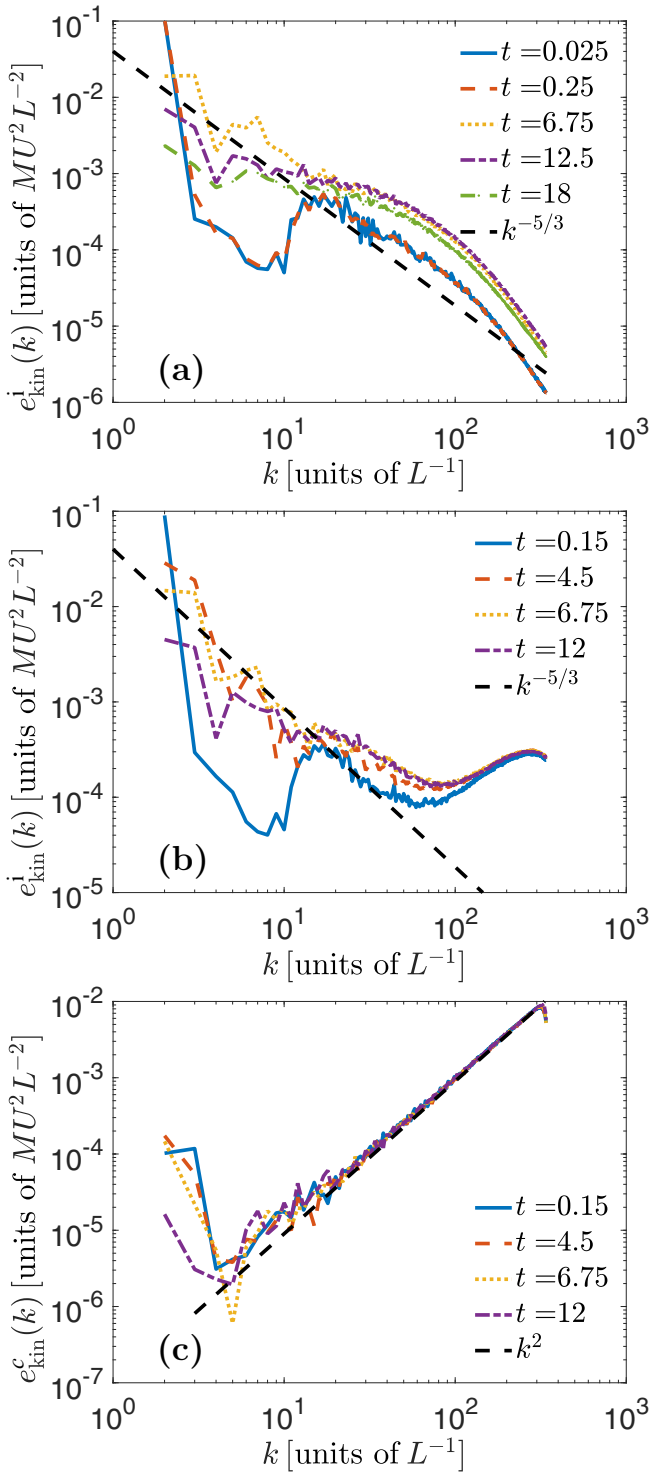

FIG. 9. Temporal evolution of the kinetic energy spectra: (a) incompressible component $e^i_{\rm kin}(k)$ at $T = 0$; (b) incompressible component $e^i_{\rm kin}(k)$; and (c) compressible component $e^c_{\rm kin}(k)$, for the TGPE run at $T = 0.33\,T_\lambda$ with linear spatial resolution $N = 1024$ and $\xi k_{\rm max} = 2.5$. The energy spectra are in units of MU^2L^{-2} and k in units of L^{-1}.

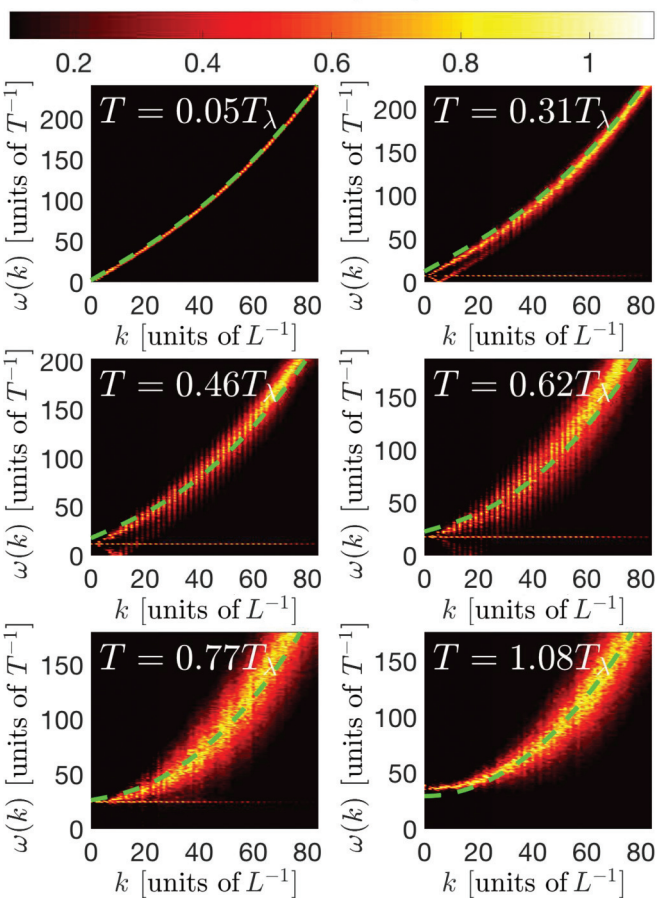

FIG. 10. Spatiotemporal spectra with $\xi k_{\rm max} = 1.5$ and $N = 256^3$, for different temperatures as indicated in each panel. The (green) dashed line indicates the theoretical Bogoliubov dispersion relation. Bright (red to yellow) areas indicate modes with large excitation. The frequency $\omega(k)$ is given in units of T^{-1}, and k is in units of L^{-1}.

In Figs. 13(a)–13(c) we show the plots of $\lambda(k, T)$ vs k from our simulations for different values of temperatures (below and above T_λ) for $\xi k_{\rm max} = 1.5$, 2.5, and 4, respectively. The dispersion relation at different temperatures was directly measured from the STS in Fig. 11. We find that $\lambda(k, T)$ in many cases, for wave numbers larger than $k \approx 1/\xi$, has a tendency to either saturate or fluctuate around a mean value. For simplicity, we approximate the mean-free path at each temperature by taking $\lambda(T) = \lambda(k \approx k_{\rm max}, T)$. In Fig. 14(a) we show the plot of $\lambda(T)$ vs T for three different values of $\xi k_{\rm max} = 1.5$, 2.5, and 4; we find that $\lambda(T)$ decreases as we increase the temperature. Also, in general, it increases with $\xi k_{\rm max}$, i.e., reduction in the nonlinear interaction strength.

From the mean-free path, we estimate the effective viscosity by writing

$$\nu_{\rm eff}(T) \sim \lambda(T)\left.\frac{d\omega_B}{dk}\right|_{k\approx k_{\rm max}} = \frac{\left(\left.\frac{d\omega_B}{dk}\right|_{k\approx k_{\rm max}}\right)^2}{\Delta\omega(k \approx k_{\rm max}, T)}, \qquad (40)$$

wherein we evaluate $\Delta\omega(T)$ and $d\omega_B/dk$ at $k = 80 \approx k_{\rm max}$. In Fig. 14(b) we show the temperature dependence of $\nu_{\rm eff}(T)$, wherein we have normalized it by the quantum of circulation $4\pi\alpha = 4\pi c\xi\sqrt{2}$. For temperatures above $0.5T_\lambda$, both λ and

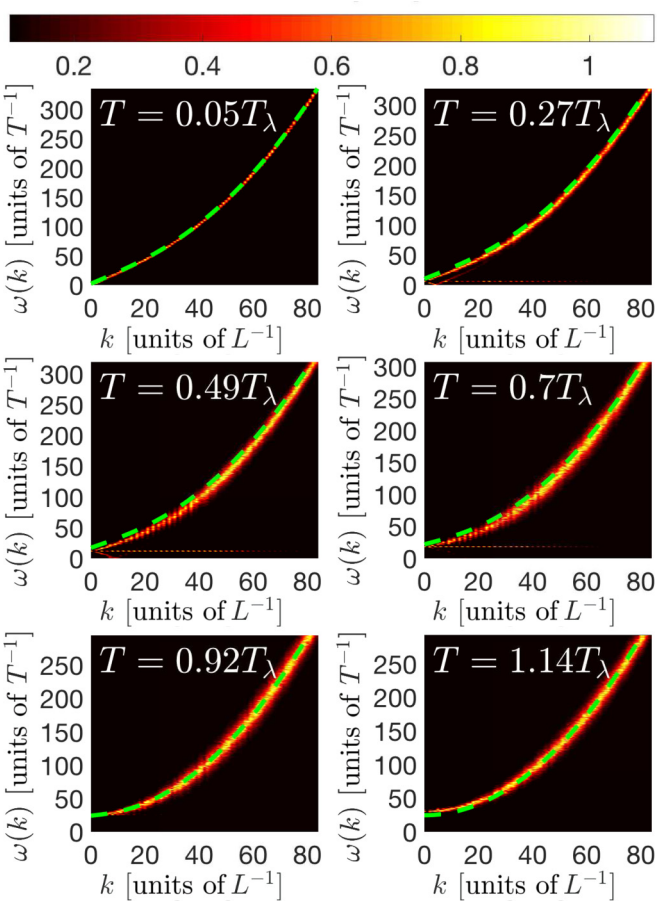

FIG. 11. Spatiotemporal spectra with $\xi k_{\max} = 2.5$ and $N = 256^3$, for different temperatures as indicated in each figure. The (green) dashed line indicates the theoretical Bogoliubov dispersion relation. Bright (red to yellow) areas indicate modes with large excitation. The frequency $\omega(k)$ is given in units of T^{-1}, and k is in units of L^{-1}.

$\nu_{\rm eff}$ are roughly constant. For the runs with $\xi k_{\max} = 2.5$, we have

$$\lambda(T) \sim 10\xi, \tag{41}$$

$$\nu_{\rm eff}(T) \sim 50\alpha = 50c\xi/\sqrt{2}. \tag{42}$$

We emphasize that Eq. (42) provides an estimate of the effective viscosity in terms of physical parameters: the speed of sound c and the healing length. Therefore, for the simulations with $c = 2U$ and $\xi = 2.5/k_{\max} = 2.5 \times 3L/N$, we write the effective viscosity as

$$\nu_{\rm eff}(T) \sim LU\frac{500}{N}, \tag{43}$$

where U and L are the unit velocity and length, and N is the linear spatial resolution. In dimensionless units, with $U = L = 1$, we obtain an estimate of the Reynolds number as

$$\mathrm{Re}^{(\mathrm{TG})} = \frac{C}{\nu_{\rm eff}} = \frac{CN}{500}, \tag{44}$$

where C is a prefactor of order unity. We remark that $\nu_{\rm eff}$ is an effective transport coefficient; we can ascertain its value from

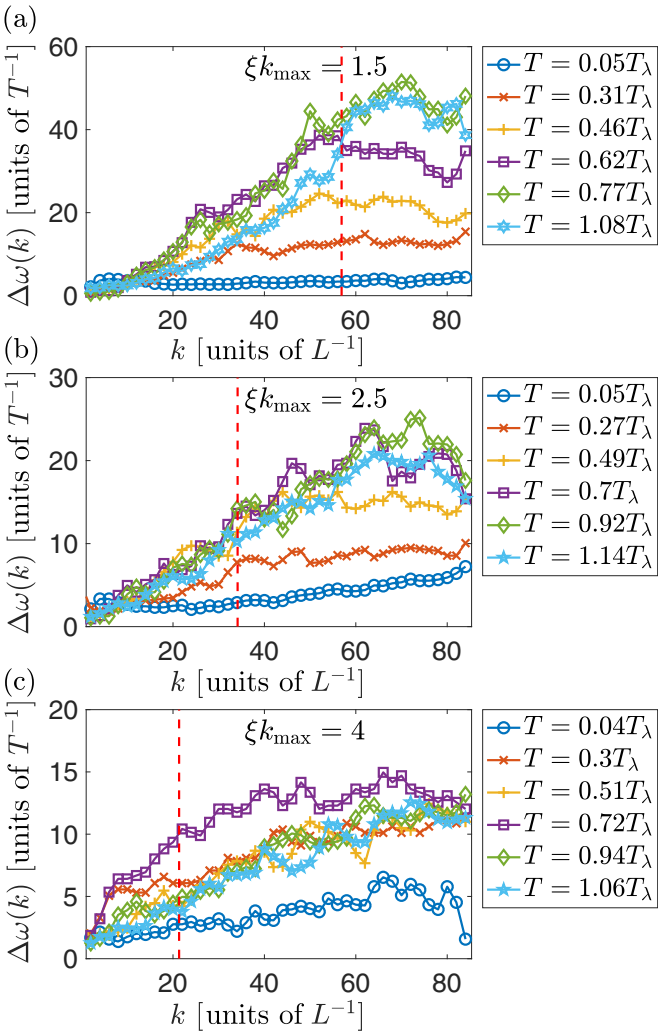

FIG. 12. Spectral broadening $\Delta\omega(k)$ of the dispersion relation, for different temperatures and values of $\xi k_{\max}$. The vertical dashed lines indicate the value of $1/\xi$ in each case: (a) as a function of k for different temperatures and for $\xi k_{\max} = 1.5$, (b) same for $\xi k_{\max} = 2.5$, and (c) same for $\xi k_{\max} = 4$. The frequency $\Delta\omega(k)$ is given in units of T^{-1}, and k is in units of L^{-1}.

the mean-free path only up to a multiplicative constant. Also, $\mathrm{Re} \sim 1/\nu_{\rm eff}$ is the usual definition of the Reynolds number in numerical studies of the Taylor-Green flow [43].

In Sec. III F we provide a comparison of the GPE runs with DNSs of the Navier-Stokes equations at low Reynolds numbers; therefore, for convenience we give yet another definition of the Reynolds number based on the dynamic root mean square (r.m.s.) flow velocity

$$U_0 = \sqrt{2E} \tag{45}$$

and the flow correlation length

$$L_0 = 2\pi\,\frac{\int E(k)/k\,dk}{\int E(k)\,dk} \tag{46}$$

(i.e., the flow integral scale). Moreover, if we write U_0 and L_0 in units of U and L, the Reynolds number is

$$\mathrm{Re} = C\frac{U_0L_0}{\nu_{\rm eff}} = C\frac{U_0L_0N}{500}. \tag{47}$$

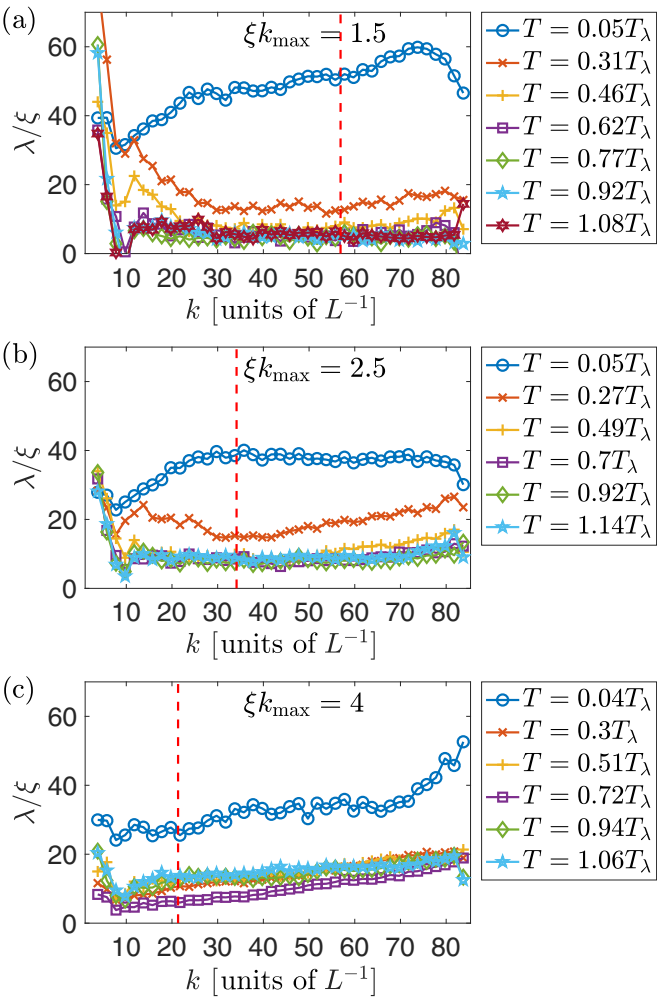

FIG. 13. Mean-free path as a function of k for different temperatures in simulations with $\xi k_{\max} = 1.5$ (a), $\xi k_{\max} = 2.5$ (b), and $\xi k_{\max} = 4$ (c). The vertical dashed line indicates the value of $1/\xi$. The wave number k is given in units of L^{-1}.

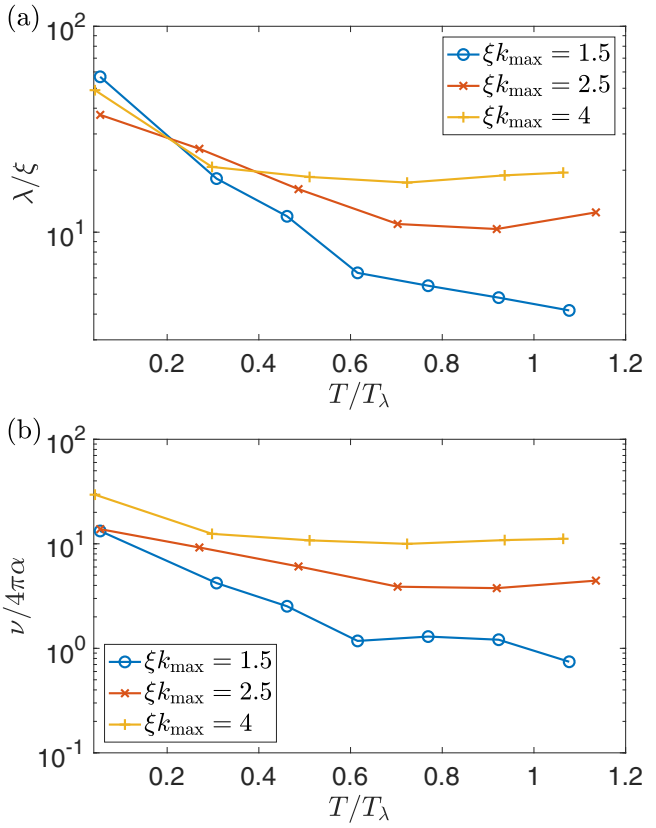

FIG. 14. (a) Mean free-path as a function of temperature T for different values of $\xi k_{\max}$. (b) Effective viscosity (acting on the normal fluid), normalized by the quantum of circulation $4\pi\alpha = 4\pi c\xi/\sqrt{2}$, as a function of temperature T for different values of $\xi k_{\max}$.

It is worth reiterating that $\nu_{\rm eff}(T)$ depends on the value of $\xi k_{\max}$; the nonlinear interaction strength decreases, if we increase $\xi k_{\max}$. Therefore, in simulations with $\xi k_{\max} = 1.5$ we have a stronger turbulence than in the case of $\xi k_{\max} = 2.5$. Moreover, the mean-free path (see Fig. 14) in the runs with $\xi k_{\max} = 1.5$ is $\lambda(T) \sim 5\xi$, which gives a smaller $\nu_{\rm eff}(T) \sim 15\alpha$. Therefore, a larger Reynolds number

$$\mathrm{Re} = C\frac{U_0 L_0}{\nu_{\rm eff}} = C\frac{U_0 L_0 N}{90}. \tag{48}$$

However, we cannot arbitrarily decrease $\xi k_{\max}$ to obtain higher values of Re. At a fixed spatial resolution, $\xi k_{\max}$ must be larger than unity if we want to properly resolve the vortices in simulations.

In a two-fluid framework, the viscosity in Eq. (43) corresponds to a viscosity acting on the normal fluid (as it was obtained from the thermalized component). This is consistent with derivations of damping from stochastic equations for quasiclassical fields (see, e.g., [31,32]), where modes below an energy cutoff are considered as the condensate, and modes above the cutoff are considered as thermalized noise. In our case, the distinction is made using the STS, and from an extraction of the excitations lying in the vicinity of the dispersion relation of the waves. Therefore, at very high temperatures we basically have one fluid with viscosity $\nu_{\rm eff}$. At intermediate temperatures, if the mutual friction is large enough, the two fluids are then locked together. Mutual friction in this case is estimated to be proportional to ρ_n/ρ_0 (see [37]). Thus, at intermediate temperatures we can assume that the two fluids are locked with an effective mutual viscosity

$$\nu'_{\rm eff} = \frac{\rho_n(T)}{\rho_0}\nu_{\rm eff}(T). \tag{49}$$

These results are consistent with the following interpretation. At temperatures close to the transition temperature, the TG flow is very viscous. In the next subsection, we provide a verification of this by performing Navier-Stokes simulations using $\nu_{\rm eff}$ and comparing them with the TGPE runs. This will also allow us to confirm that the effective Reynolds number of the finite-temperature TGPE flows are low, even for the high-resolution runs presented in this work. At the same time, this will enable us to obtain an estimate of the prefactor C in Eq. (47). Moreover, this assessment is also consistent with previous estimations based on the free decay of the incompressible kinetic energy in Ref. [42]. In fact, estimates based on Eq. (47) suggest that to obtain a turbulent normal fluid described by the TGPE near or above T_λ would require resolutions that are not achievable even in the

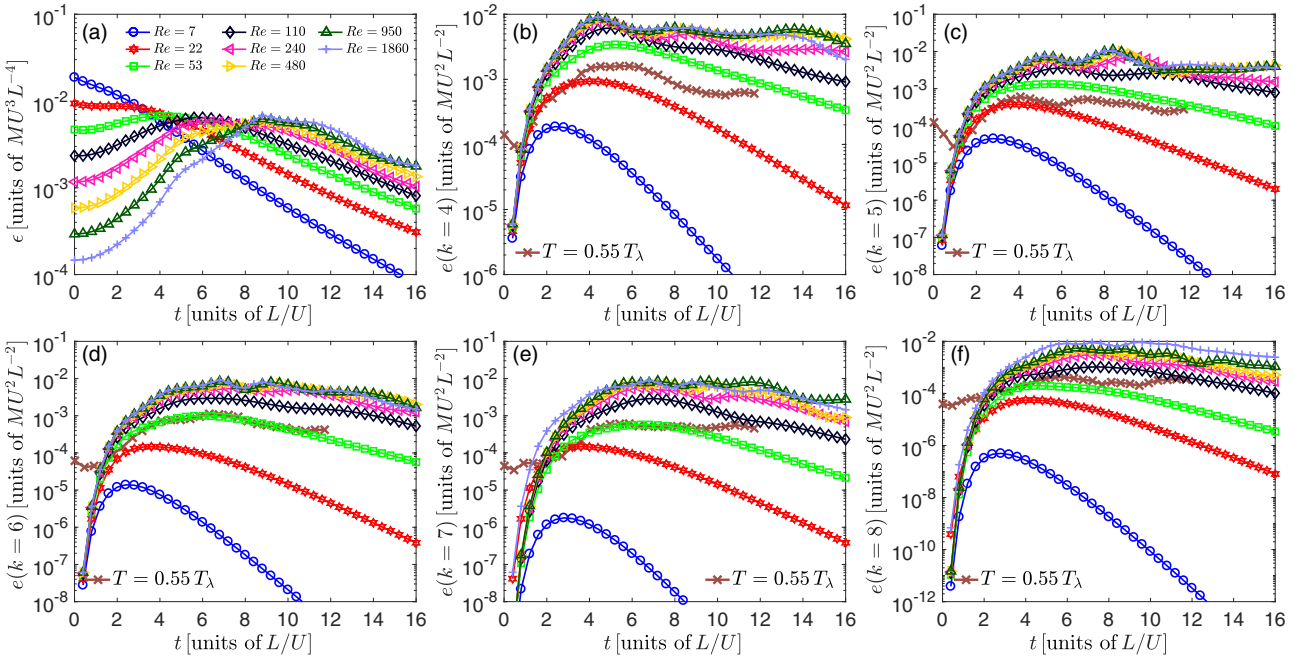

FIG. 15. Results from the DNS of low-Reynolds-number Navier-Stokes TG runs at different Reynolds numbers [Re $= U_0 L_0/\nu$, based on the integral scale L_0 and the flow r.m.s. velocity U_0; see Eqs. (45) and (46)]. (a) Plots of energy dissipation rate ϵ vs time. The maximum of ϵ for the run with Re $= 1860$ occurs at $t \approx 9\,L/U$. (b)–(f) Plots of the temporal evolution of the energy in different k shells in Fourier space [i.e., $e(k,t)$ for fixed k as a function of time] for $k = 4$ to 8 from the Navier-Stokes TG runs and the TGPE run at temperature $T = 0.55\,T_\lambda$ [linear resolution $N = 1024$ and $\xi k_{\rm max} = 2.5$; for GPE $e(k,t)$ corresponds to $e^i_{\rm kin}(k,t)$]. In all panels, the GPE run at $T = 0.55\,T_\lambda$ is indicated by the (brown) curve with crosses, while all Navier-Stokes runs at different Reynolds numbers are labeled as indicated in (a). To vary the Reynolds numbers, the Navier-Stokes runs were performed with kinematic viscosities $\nu = 1/10$ and $1/40$ at linear spatial resolutions $N = 64$; $\nu = 1/80$ and $1/160$ ($N = 128$); $\nu = 1/320$, $1/640$, and $1/1280$ ($N = 256$); $\nu = 1/2560$ ($N = 512$). The energy spectra components are given in units of MU^2L^{-2}, and time is in units of L/U.

largest supercomputers available today. Therefore, performing a classical turbulent Navier-Stokes simulation with the TGPE is prohibitively expensive!

At small temperatures we have a system that can be modeled either with the Euler and Boltzmann equations with small coupling or, more formally, with a stochastic equation for a quasiclassical field [32] (the system being close to GPE dynamics). Finally, in the intermediate temperature range, the system can be represented by coupled Euler and Navier-Stokes fluids; we leave its modeling for future works.

F. Comparisons with low Reynolds runs

To verify that the evolution of a finite-temperature TG flow is similar to a highly viscous classical flow, and to estimate the value of the factor C in Eq. (47), we perform a set of simulations of freely decaying "classical" TG flows obeying the Navier-Stokes equations at different Reynolds numbers Re $= U_0 L_0/\nu = 7$ (with a spatial resolution $N^3 = 64^3$), 22 ($N^3 = 64^3$), 53 ($N^3 = 128^3$), 110 ($N^3 = 128^3$), 240 ($N^3 = 256^3$), 480 ($N^3 = 256^3$), 950 ($N^3 = 256^3$), and 1860 ($N^3 = 512^3$). Here, ν is the kinematic viscosity; the r.m.s. flow velocity U_0 and the flow correlation length L_0 are the time-averaged values, between $t = 4$ and 10, in a developed turbulence state. We compare these runs with the TGPE run at $T = 0.55\,T_\lambda$ for $\xi k_{\rm max} = 2.5$ on $N^3 = 1024^3$ collocation points.

In Fig. 15(a) we show the time evolution of the energy dissipation rate ϵ for these TG Navier-Stokes runs. We observe that as we increase Re, the time to achieve the maximum energy dissipation rate also increases, after which turbulence develops. To provide a detailed comparison between the runs, in Figs. 15(b)–15(f) we show the temporal evolution of the incompressible kinetic energy in Fourier shells $k = 4\,L^{-1}$ to $8\,L^{-1}$, respectively, for the above-mentioned Navier-Stokes runs and for the TGPE run. We find it remarkable that the shell-by-shell evolution of these two systems shows a considerable overlap for Reynolds numbers in the range Re $= 22$ to 53; in other words, the time evolution of the energy in each shell in the TGPE run is in-between these two Navier-Stokes runs. This is in reasonable agreement, at least in terms of order of magnitude, with the predictions given by Eq. (47). We compute L_0 and U_0 for the TGPE run averaged over the time interval $t = 4$ to 10, as in the case if TG Navier-Stokes runs, we obtain Re $= 5C$; this suggests that $C \approx 7$.

IV. CONCLUSION

The results presented in this paper significantly extend our knowledge of quantum turbulence in the Taylor-Green vortex flows. At zero temperature, runs with linear spatial resolutions up to $N = 4096$ grid points allowed us to characterize the presence of a Kolmogorov scaling range at scales larger than the intervortex distance ℓ, and to observe another scaling range at scales smaller than ℓ. The

presence of tangled substructures is apparent in vortex line visualizations.

We use the thermal equilibria and spatiotemporal spectra (i) to separate the condensed phase from the interacting waves, (ii) to estimate the mean-free path and the effective viscosity as a function of temperature from the nonlinear broadening. The actual (large) values of our estimated effective viscosity near the λ transition $\nu_{\rm eff} \sim 500/N$ (in dimensionless units) for $\xi k_{\rm max} = 2.5$, and $\nu_{\rm eff} \sim 90/N$ for $\xi k_{\rm max} = 1.5$, correspond to effective Reynolds numbers ${\rm Re} \sim U_0 L_0 N/500$ and ${\rm Re} \sim U_0 L_0 N/90$ (up to prefactors of order unity), respectively, where N is the linear resolution of the simulation.

Finally, the comparison of finite-temperature quantum turbulence at $N = 1024$ grid points with the low-Reynolds Navier-Stokes numerical simulations further confirms our estimations of the effective viscosity $\nu_{\rm eff}$ based on the mean-free path of the thermal excitations, and allows us to determine the amplitude of the unknown prefactors.

It is well known (see, e.g., Ref. [43]) that Kolmogorov scaling becomes apparent in the Navier-Stokes numerical simulations of the Taylor-Green flow with linear resolutions of $N = 256$, for ${\rm Re} \approx 1600$. We can thus conclude that an equivalent direct numerical simulation using the truncated Gross-Pitaevskii equation performed at $T \approx T_\lambda$ would need a resolution of about $N \approx 10\,000$ grid points in each spatial direction for $\xi k_{\rm max} = 1.5$, and of $N \approx 43\,000$ for $\xi k_{\rm max} = 2.5$, to achieve a similar Reynolds number and a classical direct energy cascade with similar scale separation for the normal fluid. These resolutions are out of reach using present day computing resources. At smaller values of T, this situation changes drastically, as the mutual friction between the fluid and the superfluid depends on the density fraction of the normal fluid as ρ_n/ρ_0 [37].

Looking back at the estimates of effective viscosity, it can be seen that the high value of $\nu_{\rm eff}$ traces back to the high value of $(d\omega_B/dk)^2/\Delta\omega$ at $k = k_{\rm max}$ for the Gross-Pitaevskii equation. This brings into mind the possibility of modifying the Bogoliubov dispersion relation through modifications in Gross-Pitaevskii, and thereby changing the value of $(d\omega_B/dk)^2$ at high wave numbers. It is well known that by changing the cubic term in the Gross-Pitaevskii equation into a nonlocal term of the form $\psi \int |\psi(\mathbf{x}')|^2 V(|\mathbf{x} - \mathbf{x}'|)\, d\mathbf{x}'$, the first term in the Bogoliubov dispersion relation can be changed to a term involving a potential $\widetilde{V}(k) = \int V(r) \exp[-i\mathbf{k}\cdot\mathbf{r}]\, d\mathbf{r}$. In this way, it is possible to "adjust" the dispersion relation [see, e.g., Eqs. (3) and (4) of Ref. [35]]. This approach, aside from allowing for the modeling of rotons in superfluid ^{4}He at low temperatures, can also lead to a decrease in the values of effective viscosity at temperatures close to the λ transition. The impact of these changes in $\nu_{\rm eff}$ is left for future work.

ACKNOWLEDGMENTS

The authors acknowledge financial support from ECOS-Sud Grant No. A13E01, and computing hours in the IDRIS supercomputer granted by Project No. IDRIS 100591 (No. DARI x20152a7493). Computations were also carried out on the Mésocentre SIGAMM hosted at the Observatoire de la Côte d'Azur. P.C.dL. acknowledges funding from the European Research Council under the European Community's Seventh Framework Program, ERC Grant Agreement No. 339032. P.D.M. acknowledges funding from Grant PICT No. 2015-3530, and useful discussions with E. Calzetta. G.K. was supported by Agence Nationale de la Recherche through the project GIANTE ANR-18-CE30-0020-01.

[1] R. P. Feynman, in *Progress in Low Temperature Physics*, edited by C. J. Gorter (Elsevier, Amsterdam, 1955), Vol. 1, pp. 17–53.
[2] R. J. Donnelly, *Quantized Vortices in Helium II* (Cambridge University Press, Cambridge, 1991).
[3] C. F. Barenghi, L. Skrbek, and K. R. Sreenivasan, Proc. Natl. Acad. Sci. USA **111**, 4647 (2014).
[4] W. F. Vinen and J. J. Niemela, J. Low Temp. Phys. **128**, 167 (2002).
[5] V. Tsepelin, A. W. Baggaley, Y. A. Sergeev, C. F. Barenghi, S. N. Fisher, G. R. Pickett, M. J. Jackson, and N. Suramlishvili, Phys. Rev. B **96**, 054510 (2017).
[6] E. A. L. Henn, J. A. Seman, G. Roati, K. M. F. Magalhães, and V. S. Bagnato, Phys. Rev. Lett. **103**, 045301 (2009).
[7] C. Nore, M. Abid, and M. E. Brachet, Phys. Rev. Lett. **78**, 3896 (1997).
[8] J. Maurer and P. Tabeling, Europhys. Lett. **43**, 29 (1998).
[9] V. S. L'vov and S. Nazarenko, J. Exp. Theor. Phys. Lett. **91**, 428 (2010).
[10] L. D. Landau and E. M. Lifshitz, *Fluid Mechanics*, Course of Theoretical Physics, Vol. 6, 2nd ed. (Pergamon, Amsterdam, 2012).
[11] H. E. Hall and W. F. Vinen, Proc. R. Soc. London A **238**, 204 (1956).
[12] I. Bekarevich and I. Khalatnikov, J. Exptl. Theoret. Phys (U.S.S.R.) **40**, 920 (1961) [Sov. Phys.–JETP **13**, 643 (1961)].
[13] P.-E. Roche, C. F. Barenghi, and E. Leveque, Europhys. Lett. **87**, 54006 (2009).
[14] V. Shukla, A. Gupta, and R. Pandit, Phys. Rev. B **92**, 104510 (2015).
[15] L. Biferale, D. Khomenko, V. L'vov, A. Pomyalov, I. Procaccia, and G. Sahoo, Phys. Rev. Fluids **3**, 024605 (2018).
[16] D. H. Wacks and C. F. Barenghi, Phys. Rev. B **84**, 184505 (2011).
[17] L. Boué, V. L'vov, A. Pomyalov, and I. Procaccia, Phys. Rev. Lett. **110**, 014502 (2013).
[18] L. Boué, V. S. L'vov, Y. Nagar, S. V. Nazarenko, A. Pomyalov, and I. Procaccia, Phys. Rev. B **91**, 144501 (2015).
[19] V. Shukla and R. Pandit, Phys. Rev. E **94**, 043101 (2016).
[20] K. W. Schwarz, Phys. Rev. B **31**, 5782 (1985).
[21] A. W. Baggaley, J. Laurie, and C. F. Barenghi, Phys. Rev. Lett. **109**, 205304 (2012).
[22] D. Khomenko, L. Kondaurova, V. S. L'vov, P. Mishra, A. Pomyalov, and I. Procaccia, Phys. Rev. B **91**, 180504 (2015).
[23] J. Koplik and H. Levine, Phys. Rev. Lett. **71**, 1375 (1993).
[24] C. Nore, M. Abid, and M. E. Brachet, Phys. Fluids **9**, 2644 (1997).

[25] U. Frisch, *Turbulence: The Legacy of A. N. Kolmogorov* (Cambridge University Press, Cambridge, 1995).
[26] M. Kobayashi and M. Tsubota, Phys. Rev. Lett. **94**, 065302 (2005).
[27] P. Clark di Leoni, P. D. Mininni, and M. E. Brachet, Phys. Rev. A **92**, 063632 (2015).
[28] A. Villois, D. Proment, and G. Krstulovic, Phys. Rev. E **93**, 061103 (2016).
[29] P. Clark di Leoni, P. D. Mininni, and M. E. Brachet, Phys. Rev. A **95**, 053636 (2017).
[30] A. Brissaud, U. Frisch, J. Leorat, M. Lesieur, and A. Mazure, Phys. Fluids (1958-1988) **16**, 1366 (1973).
[31] C. W. Gardiner and P. Zoller, Phys. Rev. A **61**, 033601 (2000).
[32] C. W. Gardiner, J. R. Anglin, and T. I. A. Fudge, J. Phys. B: At., Mol. Opt. Phys. **35**, 1555 (2002).
[33] E. Calzetta, B. L. Hu, and E. Verdaguer, Int. J. Mod. Phys. B **21**, 4239 (2007).
[34] N. P. Proukakis and B. Jackson, J. Phys. B: At., Mol. Opt. Phys. **41**, 203002 (2008).
[35] N. G. Berloff, M. Brachet, and N. P. Proukakis, Proc. Natl. Acad. Sci. USA **111**, 4675 (2014).
[36] M. J. Davis, S. A. Morgan, and K. Burnett, Phys. Rev. Lett. **87**, 160402 (2001).
[37] G. Krstulovic and M. Brachet, Phys. Rev. E **83**, 066311 (2011).
[38] G. Krstulovic and M. Brachet, Phys. Rev. Lett. **106**, 115303 (2011).
[39] V. Shukla, M. Brachet, and R. Pandit, New J. Phys. **15**, 113025 (2013).
[40] R. Pandit, D. Banerjee, A. Bhatnagar, M. Brachet, A. Gupta, D. Mitra, N. Pal, P. Perlekar, S. S. Ray, V. Shukla *et al.*, Phys. Fluids **29**, 111112 (2017).
[41] V. Shukla, M. Brachet, and R. Pandit, arXiv:1412.0706.
[42] P. Clark Di Leoni, P. D. Mininni, and M. E. Brachet, Phys. Rev. A **97**, 043629 (2018).
[43] M. E. Brachet, D. I. Meiron, S. A. Orszag, B. G. Nickel, R. H. Morf, and U. Frisch, J. Fluid Mech. **130**, 411 (1983).
[44] D. Gottlieb and S. A. Orszag, *Numerical Analysis of Spectral Methods* (SIAM, Philadelphia, 1977).
[45] C. Calvin, Parallel Comput. **22**, 1255 (1996).
[46] P. Dmitruk, L.-P. Wang, W. H. Matthaeus, R. Zhang, and D. Seckel, Parallel Comput. **27**, 1921 (2001).
[47] D. O. Gómez, P. D. Mininni, and P. Dmitruk, Phys. Scr. **T116**, 123 (2005).
[48] P. Mininni, D. Rosenberg, R. Reddy, and A. Pouquet, Parallel Comput. **37**, 316 (2011).
[49] A. C. White, B. P. Anderson, and V. S. Bagnato, Proc. Natl. Acad. Sci. USA **111**, 4719 (2014).
[50] M. C. Tsatsos, P. E. S. Tavares, A. Cidrim, A. R. Fritsch, M. A. Caracanhas, F. E. A. dos Santos, C. F. Barenghi, and V. S. Bagnato, Phys. Rep. **622**, 1 (2016).
[51] G. Krstulovic, Phys. Rev. E **86**, 055301 (2012).
[52] V. S. L'vov, S. V. Nazarenko, and O. Rudenko, Phys. Rev. B **76**, 024520 (2007).
[53] J. Clyne, P. Mininni, A. Norton, and M. Rast, New J. Phys. **9**, 301 (2007).
[54] See Supplemental Material at http://link.aps.org/supplemental/10.1103/PhysRevA.99.043605 for videos M1 and M2 that show the time evolution of incompressible kinetic energy spectra compensated by the Kolmogorov scaling at zero and finite temperatures, respectively.
[55] P. Clark di Leoni, P. J. Cobelli, P. D. Mininni, P. Dmitruk, and W. H. Matthaeus, Phys. Fluids **26**, 035106 (2014).
[56] P. C. Clark di Leoni, P. J. Cobelli, and P. D. Mininni, Eur. Phys. J. E **38**, 1 (2015).
[57] S. Nazarenko, *Wave Turbulence* (Springer, Berlin, 2011).